NASA INNOVATIVE ADVANCED CONCEPTS (NIAC) – Phase I

Grant Number 80NSSC18K0911

Rotary-Motion-Extended Array Synthesis (R-MXAS) FINAL REPORT

Principal Investigator: Dr. John R. Kendra
Leidos, Inc.

(U) March 25, 2019

(U) Prepared By:
Leidos Innovations Corporation
14668 Lee Road
Chantilly, VA 20151

TABLE OF CONTENTS

LIST OF FIGURES / TABLES

1.0 INTRODUCTION

1.1 INNOVATION: ROTARY MOTION EXTENDED ARRAY SYNTHESIS (R-MXAS)

R-MXAS is a revolutionary aerospace architecture for realizing a synthetic aperture imaging radiometer (SAIR) with dramatically lower SWaP than existing state-of-the-art (SOTA) methods. The space-based component of the R-MXAS system (Figure 1) is a single platform comprising a 1-D sparse / decimated antenna array on a rigid tether (deployed parallel to the horizon) and one or more additional tethered antennas that rotate in a plane orthogonal to the 1-D array. The processing that correlates the data from these two antenna systems and performs image reconstruction has both space-based and ground-based components. The processing exploits the interferometric baselines formed between the rotating tethered antenna at radius R and each of the antennas of the 1-D array on the rigid tether. This is illustrated in Figure 2(a) which shows a single interferometric baseline produced between the rotating antenna element (a single antenna, not an array in this version of the concept) and a particular antenna element on the rigid boom. Figure 2(b) and

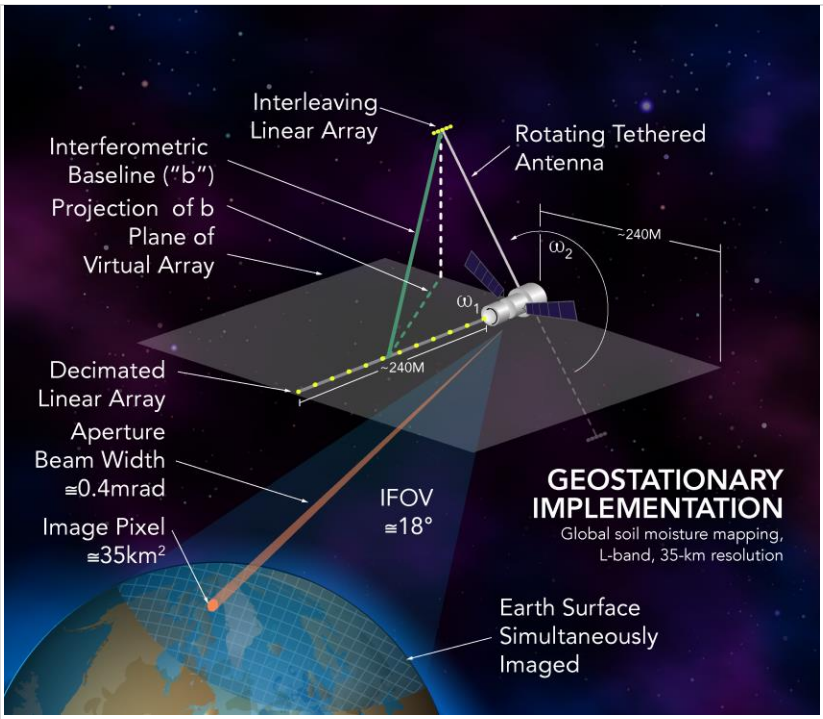

Figure 1: R-MXAS concept for earth remote sensing from geostationary orbit. *The illustration depicts the R-MXAS system overlooking the earth. A beam from the center of the system illuminates the disk of the earth, and the earth surface within this beam is covered with a gridded transparent film suggesting imaging. A much narrower beam from the R-MXAS system illuminates just one of the pixels indicating the spatial resolution of the system. The R-MXAS system has a rigid boom of length 240m having a 1-D sparse array, lying in the plane of, and bisecting, a large virtual aperture oriented orthogonal to a normal to the earth disk. An additional boom or tether with radius 240m rotates in a plane orthogonal to the virtual aperture plane. The tether extends from both sides of the central hub, and there is a small antenna array at each of the tether ends. The hub is located at one edge of the virtual aperture plane, at the line of bisection. An example interferometric baseline is shown extending from one antenna element on the rigid boom to one of the rotating antennas, for a rotation angle that is ~$\mathbf{45}^{\circ}$ relative to the virtual aperture plane. The projection of this baseline into the plane is highlighted.*

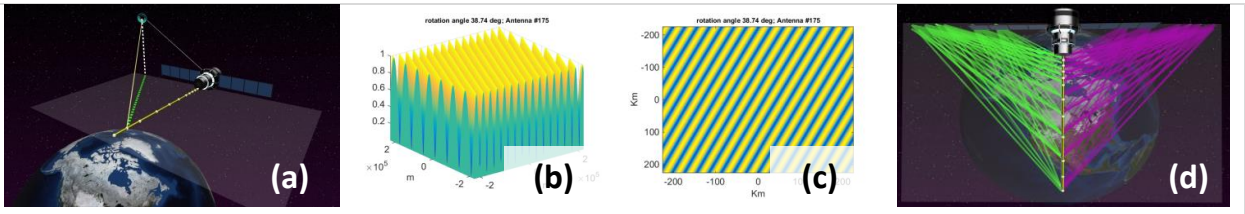

Figure 2: R-MXAS Baseline and spatial basis function detail. *A) A particular baseline is depicted, very similar to that of Figure 1; B) a 3D rendering of the computed spatial basis function on the surface of the earth cast/measured by the baseline, a sinusoidal fringe pattern with an orientation of ~$\mathbf{45}^{\circ}$; C) a 2D representation of the basis function, appearing as alternating bright and dark regions; d) illustration, using a top view of the Figure 1 R-MXAS system, of a large set of projected baselines that are formed from multiple rotational positions and multiple fixed antennas.*

2(c) show the spatial basis function associated with the out-of-plane baseline, as it manifests on the earth. Due to the antenna rotation, the projections of these baselines into the horizontal plane containing the rigid tether engender a continuum of *along-track* baselines which range in length from zero to *R*. Figure 2(d) illustrates a collection of such projected baselines that are created from multiple rotation positions and for multiple fixed antenna elements. The maximum along-track baseline is thus given by the length of the rotating tether, and the maximum *across-track* baseline is given by the length of the rigid tether. The Phase I research has shown that a fully populated u-v plane, with zero redundancy, though very high density, is realized by this process in one quarter rotation of the rotating tether, assuming, as shown in Figure 1, a balanced antenna design, with antenna(s) at either end of the tether.

1.2 MISSION CONTEXT: GLOBAL SOIL MOISTURE MONITORING

A relevant mission context is global soil moisture monitoring, in which context we can also find the SOTA for a large RF aperture in space. This is seen for example in the European Space Agency's (ESA's) low earth orbit (LEO) Soil Moisture and Ocean Salinity (SMOS) mission [1],[2], which since its launch in 2009 has been providing global volumetric soil moisture (SM) estimates, at a ground resolution of approximately 35-km. These SM estimates significantly enhance meteorological and hydrological models applicable to weather and climate prediction, as well allowing for the monitoring of potential drought and flooding scenarios.

The SMOS payload is a sparse Y-shaped array (Figure 3), each 4-m arm of which contains 23 L-band antennas operating in a 20-MHz band around 1.4 GHz. To illustrate the technical credibility of R-MXAS in a relevant and game-changing mission context, our Phase I research investigated an implementation of R-MXAS that would be capable of executing the global SM mapping mission from a geostationary orbit (GEO) instead of LEO, achieving the same spatial resolution of the current mission, ~35-km. A GEO orbit affords significant advantages to LEO in terms of simultaneous, full earth-disk (i.e. synoptic) measurement and a much shorter re-visit (re-image) time. For comparison, the operational SMOS mission images a swath that is roughly 1000km wide and revisits a location on the earth once every 1-3 days. In Section 5.1 we present a quantitative comparison of an R-MXAS design and a GEO-based Y-design, the latter being a scaled up version of the current SMOS mission system. Preceding that, in Section 2 we present the key results of a high-fidelity data-driven simulation of the R-MXAS imaging concepts, and, in Section 3, a detailed description of the specific signal processing measures employed in the simulation. Then, in Section 4 we describe some particular innovations that emerged through the Phase I research pertaining to and benefiting antenna sparsity and radiometric sensitivity for R-MXAS. Various design attributes for R-MXAS discussed in all of these sections are brought together to inform the R-MXAS system design for GEO-based SM monitoring that is ultimately compared in Section 5.1.

Figure 3: ESA SMOS mission satellite. *A Y-shaped antenna array facing the earth, consisting of three equal arms separated from one another by* **120**$^{\circ}$*. The satellite is shown above the rim of the earth, and is also equipped with two large solar arrays extending from a central hub which itself extends above the antenna on the non-earth-facing side.*

2.0 VALIDATION OF R-MXAS IMAGING CONCEPT: SUMMARY OF KEY FINDINGS

Given the highly non-conventional appearance and approach, the most immediate research questions surrounding the R-MXAS concept concerned theoretical and practical questions relating to the validity of the concept for actually performing imaging, as well as details and demonstration of the processing measures involved. Accordingly, the Phase I effort was almost exclusively focused on analysis, modelling, and simulation. In this section we summarize the primary results that emerged from a rigorous signal processing simulation of R-MXAS. The next section, Section 3, provides a detailed description of that simulation.

The foremost question was whether the baseline creation process suggested in Figure 1 could actually produce acceptable u-v plane coverage and therefore enable a well-behaved *point spread function* (PSF) suitable for imaging. A closely related research question was the actual design and demonstration of the signal processing algorithms necessary for the aperture formation and image reconstruction processes. Two particular factors of the R-MXAS concept are outside and even contrary to the existing principles commonly recognized in SAIR. These are: 1) *pronounced* out-of-plane baselines; and 2) ephemeral baselines, based on continuously and relatively rapid relative motion between antennas. To address these concerns the Phase I effort included a high-fidelity data-driven simulation of the aperture creation and image reconstruction process, using parameters consistent with a real example mission. A 20-MHz bandwidth noise signal, ten seconds in duration, was realistically propagated to the elements of an R-MXAS system resembling the characteristics illustrated in Figure 1. Signal processing measures were developed and then applied to produce all of the necessary correlations (i.e. calculate visibilities). For the image reconstruction process, appropriate spatial basis functions were numerically computed (R-MXAS is not compatible with a conventional FFT approach), modified by the visibilities, and summed to form a PSF. Figure 4 and Figure 5 show the principal results of the simulation. Figure 4(a) shows the u-v plane distribution (based on projected baselines), exhibiting overall very high density sampling, particularly for angles (the top and bottom of the figure) where the rotation is near horizontal, due to the cosine effect.

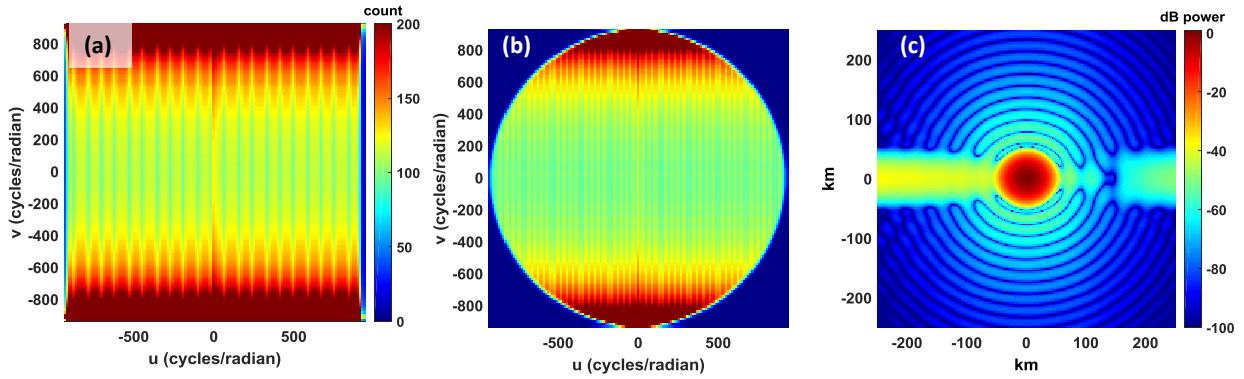

Figure 4: The R-MXAS uv-plane distribution and associated point spread function (PSF) resulting from a high-fidelity, data-driven simulation. *A) A "heat map" that is a 2-D histogram of the uv-plane density of R-MXAS baselines. It is perfectly square, and shows a sharp upturn in density at the top and bottom edge. B) A the uv-plane distribution of (A) is cropped to a circular form, the corners of the square distribution being masked. C) Topographic perspective of the PSF, following the application of a Blackman window to (B). The PSF appears as a target, with a bright center, and attenuation from the center in a mainly circularly symmetric manner. A color scale shows that the intensity drops off rapidly from main lobe, with sidelobe level ≤* **40** *dB.*

Note that, although from Figure 2(d) it may seem that R-MXAS seems to create a *triangular* distribution of (projected) baselines, it in fact engenders a perfectly square distribution as depicted in Figure 3(a). This can be understood upon considering that, in Figure 2(d), all of the baselines associated with a given element of the rigid boom array have the identical u-spatial frequency component due to that element's spatial offset, while the baselines also exhibit, collectively, a v-component that varies from zero to v_max. Thus the (green) baselines depicted in the left half plane of Figure 2(d) populate a square region (presuming equivalent lengths for the rigid boom and rotating tether) in the top left quadrant of the u-v plane, with u-max and v-max as limits; the right-half plane baselines (pink) of Figure 2(d) similarly populate the upper left half plane of the u-v plane. The lower half-plane of the u-v plane is then populated by the conjugate entities of the upper plane, leading to a completely square distribution, exactly as shown in Figure 3(a).

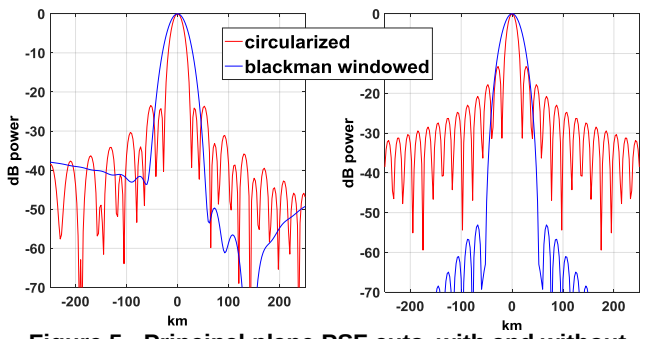

Figure 5: Principal plane PSF cuts, with and without Blackman window. *The two figures show the 2D superposition of these contours. The left figure, corresponding to a horizontal slice through the center of Figure 4(c), shows less symmetry for the Blackman window, but with sidelobe level still ≤ **40**dB. For the orthogonal cut, the right figure, the Blackman window reduces sidelobes by ~**40** dB below the non-windowed version. In both cases, the Blackman window approximately doubles the mainlobe width.*

In Figure 4(b), the u-v distribution has been circularized to promote a symmetric PSF. Figure 4(c) is topographic view of the resultant PSF, obtained after applying a Blackman window to Figure 4(b). Despite some asymmetry, the PSF is generally excellent, with sidelobe levels ≤ -40dB everywhere. The specific effect of the Blackman window is illustrated in Figure 5 which shows the principal cuts of the PSF, with and without the Blackman window applied. These results constitute evidence / proof that pronounced out-of-plane baselines manifest, in the resultant PSF, as their projections into a plane---answering a major unknown and feasibility question about the overall concept. The results further illustrate an important theme of R-MXAS; namely that sophisticated signal processing measures and computational complexity, such as is engendered by an unconventional design, may essentially be traded to achieve dramatic sparsity relative to more conventional concepts.

3.0 SIGNAL PROCESSING DESCRIPTION

In this section we discuss the signal processing theory and methods that lay at the heart of the R-MXAS concept. As has been discussed, an integral component of the Phase I research was a high-fidelity simulation of the process. This outputs of this process are illustrated in Figure 2 (spatial basis function examples for out-plane-baselines), Figure 4 (u-v plane distribution of projected baselines, PSF), and Figure 5 (resultant PSF). The simulation involves the following major steps, each of which are described in detail:

1) ***Signal Collection***: generation of a realistic (noise) signal waveform; propagation to and collection by the various receiving elements of the R-MXAS system located at GEO
2) ***Correlation***: the specific methods by which correlation products ("visibilities") are formed between the "static" antenna elements on the rigid boom and the rotating antenna(s)

3) ***Image Reconstruction***: approach by which the computed visibilities are combined with the out-of-plane interferometric baselines to enable image formation.

We note that while item (1) pertains purely to a simulation exercise, items (2) and (3) represent in preliminary form the actual processing that would be performed on mission data. The simulation scenario utilizes a 20-MHz bandwidth noise signal, modulating an RF carrier at frequency $f_c = 1.4$ GHz; this signal is emitted from the center of the earth disk and propagates to the GEO-based R-MXAS system where it is collected by that system over a time interval encompassing one half of a revolution of the rotating antenna. At a revolution rate of 3 rpm, collection occurs over a time interval of ten seconds. In this description, we consider collection both by a single rotating antenna, located at the end of a 197-m tether, as well as by a ULA of 263 antennas, having 3.5λ spacing, arranged along the length of a 197-m rigid boom.

3.1 SIGNAL COLLECTION:

The first step is generation of a noise waveform having bandwidth $B = 20$ MHz and duration of ten seconds. The baseband noise waveform complex envelope $\tilde{S}_o$ consists of normally distributed pseudorandom values, sampled at a rate of $25e^6$ complex samples per second (sps), i.e., $F_s = 25$ Msps. (For double precision values, the signal file created occupies about 2 GB of storage.) The source (emitted) RF signal is given by,

$$\tilde{S}_s(t) = \tilde{S}_o(t)exp[j(\omega t + \phi_o)], \quad (1)$$

where $j = \sqrt{-1}$, $\omega = 2\pi f_c$ is the angular frequency at L-band, and ϕ_o is the effective phase of the carrier frequency of the L-band emission, which phase we can without loss of generality consider as constant over the interval, with any variation absorbed into the phase of the complex envelope $\tilde{S}_o$.

3.1.1 Collection by Static Elements:

Representation of propagation to and collection by the static boom elements is straightforward. The baseband signal collected at element k on the rigid boom, which we denote with the subscript bk is given as:

$$\begin{aligned}\tilde{S}_{bk}(t) &= \tilde{S}_o(t-\tau_{bk})\exp[j(\omega(t-\tau_{bk})+\phi_o)]\exp[-j(\omega t+\phi_x)] \\ &= \tilde{S}_o(t-\tau_{bk})\exp[-j(\omega\tau_{bk})]\exp(j\Delta\phi),\end{aligned} \quad (2)$$

where we see that the collected signal $\tilde{S}_{bk}(t)$ is the source signal that was emitted at a time earlier by τ_{bk} where τ_{bk} is simply the time required for propagation at the speed of light between the source location and the location of element bk, that is,

$$\tau_{bk} = \frac{|\bar{r}_{bk} - \bar{r}_s|}{c}, \quad (3)$$

where $\bar{r}_{bk}$ is the location of the bk element and $\bar{r}_s$ the location of the source according to a coordinate system whose origin is arbitrary but constant. In Eq. (2), the last factor on the RHS of the first line represents the basebanding operation, in which the collected signal is mixed with the R-MXAS LO having reference phase ϕ_x; we assume that a master LO frequency is distributed to all of the receivers of the R-MXAS system so that the reference phase offset term $\Delta\phi = \phi_o - \phi_x$ is constant throughout the system and over the collection time. In addition to being a delayed copy of the source waveform, the bk -collected waveform has an additional phase term $\omega\tau_{bk}$ which is the product of the angular frequency of the carrier and the propagation distance.

3.1.2 Collection of the Rotating Elements:

The rotating antenna element is the fundamentally novel attribute of the R-MXAS concept. It is, in one way or another, responsible for the various benefits and advantages of the concept. On the other hand, it engenders significant complexity in signal processing. Attributes and parameters related to the concept of time-of-arrival, TOA, and its first and second derivatives, $\dot{TOA}$ ("*TOA-dot*") and $\ddot{TOA}$ ("*TOA-double-dot*"), require careful characterization and accommodation. This is true for the collection process, which, as we have already acknowledged, lies purely in the simulation domain. It is equally true however in the correlation processing and image reconstruction domains, exercised not only for this simulation, but also in actual mission data processing.

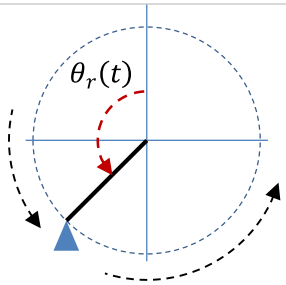

Figure 6: A 2D schematic of the rotating antenna. *Its rotational position $\boldsymbol{\theta_r(t)}$ is measured from the vertical up position, in a counter-clockwise sense.*

3.1.2.1 Delay Calculation:

The collection scenario involving a rotating antenna element is illustrated in Figure 6. To specify the received (baseband) signal as was represented for the static element bk in Eq. (2), we need to determine, for each collection time t_r the emission time $t_o(t_r)$, in a manner that accounts for the motion of the rotating antenna. Thus we have,

$$t_o(t_r) = t_r - \tau_r(t_r), \tag{4}$$

where

$$\tau_r(t_r) = \tau_{r,stat}(t_r) + \tau_{r,v}(t_r), \tag{5}$$

for which,

$$\tau_{r,stat}(t_r) = \frac{|\bar{r}_r(t_r) - \bar{r}_s|}{c} \tag{6}$$

is the *static* propagation delay from the emission source to the rotating collector position $\bar{r}_r(t_r)$, and,

$$\tau_{r,v}(t_r) = -\hat{r}_{rs}(t_r) \cdot \frac{\left[\bar{r}_r(t_r) - \bar{r}_r\left(t_r - \tau_{r,stat}(t_r)\right)\right]}{c}, \tag{7}$$

where in Eq. (7), $\hat{r}_{rs}(t_r)$ is the unit vector in the line-of-sight direction from the rotating collection element to the source, that is,

$$\hat{r}_{rs}(t_r) = \frac{[\bar{r}_r(t_r) - \bar{r}_s]}{|\bar{r}_r(t_r) - \bar{r}_s|}. \tag{8}$$

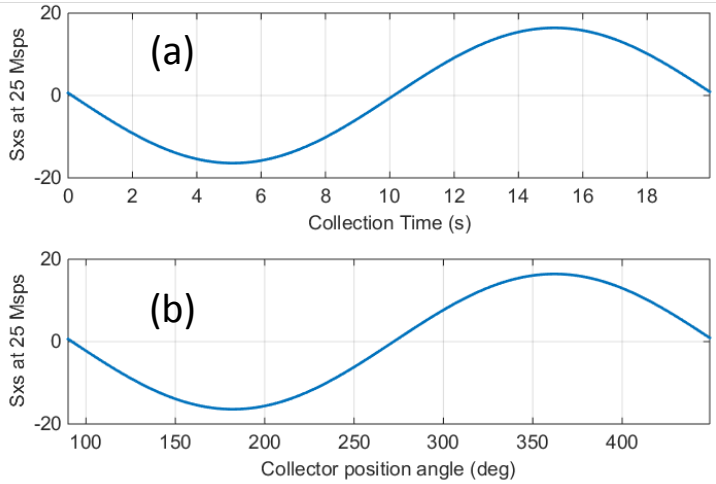

Figure 7: Emit-to-receive delay function, for a ground source and a rotating GEO-based antenna. *The 2D trace shows the differential delay to a rotating antenna at GEO, from a signal source located below it on the surface of the earth, for a complete revolution of the antenna. The differential delay is expressed as samples given a 25 Msps rate, and fluctuates in a sinusoidal manner between ~ $\pm$ **18** samples. The delay is relative to the delay for the central hub of rotation. The trace is as both a function of time, and of angular position. Note that the revolution shown begins at $\boldsymbol{\theta_r(t) = 90^{\circ}}$, based on the convention given in Figure 6.*

The explanation for Eq. (7) is that, in the time $\tau_{r,stat}(t_r)$ required for the RF waveform, travelling at the speed of light, to travel from source to point of collection, the collector itself is moving, and thus correct determination of the signal emission time relative to t_r needs to include the extra increment of signal flight time that was added or subtracted by this movement of the collector. The extra increment of time $\tau_{r,v}(t_r)$ as expressed by Eq. (7) is the radial distance, with respect to the source, travelled by the rotating antenna, divided by the speed of light.

From Figure 6 we can infer that this emission-to-collection delay value $\tau_r(t)$ is a continuously varying function of time, or equivalently, angle, $\theta_r(t)$. For the circular trajectory of the rotating antenna, given the parameters of the simulation scenario (tether and boom length, rpm, GEO location of rotation hub), it is straightforward to render this function in the form of a polynomial. To accomplish this, we compute $\tau_r(t)$ explicitly at a discrete number of points, specifically, one degree angular increments over an entire revolution, and fit these points to a polynomial. The result is shown in Figure 7**,** which shows the receive-to-collect delay, in terms of samples at F_s , over both a) time and b) collection position $\theta_r(t)$. These figures represent the time (sample) increment, positive or negative, relative to propagation to the rotation hub.

3.1.2.2 Compression / Dilation Effects:

Closely akin to the Doppler effect (in fact, mathematically equivalent as we show in Section 3.1.2.4), is the compression and dilation effects that the rotating collector engenders on the source signal. As we will show, these are $T\dot{O}A$ effects, proportional to the time derivative of $\tau_r(t)$, and they must be carefully accounted for both in this collection simulation and in correlation processing.

If we consider the source signal sampled, on the ground, at some rate F_s , then at the rotating collector, even if the sampling occurs also at F_s at that point, the very slight motion towards or away from the source yields a collected signal that has a dilated or compressed aspect relative to the source signal as it was emitted. In other words, it yields a version of the source signal that is

effectively resampled at a *very* slightly different sample rate, $F_{s,eff}(t)$, which sample rate is also a continuously-varying function of time.

As we shall see, though $F_{s,eff}(t)$ differs from F_s by a relatively tiny amount, precise accommodation of the effect is critical, in terms of both collection simulation and in terms of correlation processing of mission data. For now, we consider the collection simulation operation.

In the previous section, we described how, for a given time rotating collection position $\theta_r(t_r)$, we are able to precisely determine, armed with the polynomial function $\tau_r(t)$, the source signal that is incident, $\tilde{S}_s\big(t_r - \tau_r(t_r)\big)$. Starting at this point in the source signal stream, the collected signal is a compressed or dilated version of the signal that follows. For the purposes of a high-fidelity simulation this compressed/dilated character is achieved by resampling the source signal with an effective sample rate $F_{s,eff}(t_r)$. The value of $F_{s,eff}(t_r)$ is obtained by examining the difference in delay time $\tau_r(t)$ that occurs over one sampling interval, conducted at F_s, at the collector. That is, in a single sample time $t_s = 1/F_s$ at the collector, the effective sample rate seen for the source emission is given by

$$t_{s,eff}(t_r) = [\tau_r(t_r) - \tau_r(t_r - t_s)] + t_s \ . \tag{9}$$

In other words, $t_{s,eff}(t_r)$ is the sum of the nominal sample time t_s and the time derivative of $\tau_r(t)$, evaluated at $t = t_r$ and multiplied by t_s. That is,

$$t_{s,eff}(\mathrm{t}) = \frac{\partial}{\partial t}\big(\tau_r(t)\big) \times t_s + t_s \ , \tag{10}$$

and,

$$F_{s,eff}(t) \ = \frac{1}{t_{s,eff}(\mathrm{t})} . \tag{11}$$

Since $F_{s,eff}(t)$ and F_s are large numbers (e.g. ~25 Msps) which differ by a very small amount, in Figure 8 we show only the fractional part of the ratio of these parameters, i.e., $F_{s,eff}(t)/F_s - 1$. As expected, $F_{s,eff}(t)$ takes on its largest value when the radial velocity is directly towards the source (i.e., $\theta_r = 90^\circ$), and is zero at $\theta_r = 180^\circ$ where there is no radial velocity component in the collector motion. Note that the maximum value of $F_{s,eff}(t)$ corresponds to a dilated version of the source signal being collected, and its minimum value to a compressed version. Also, from Figure 8**,** the *rate* of change of $F_{s,eff}(t)$ is maximum at $\theta_r = 180^\circ$and zero at $\theta_r = 90^\circ$ and 270°.

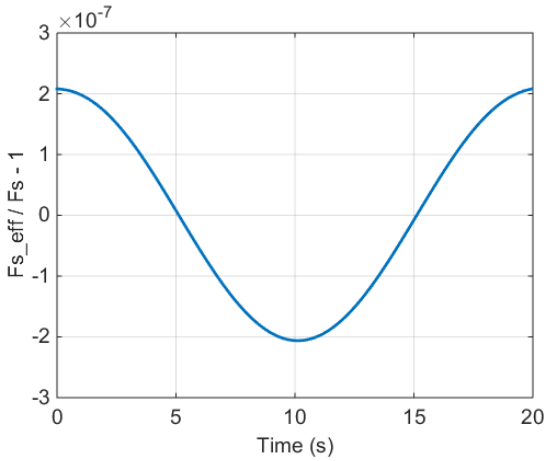

Figure 8: Fractional variation in effective sample rate of a ground-emitted signal received by the R-MXAS rotating antenna. *The 2D trace is plotted vs. time for a full revolution (20s at 3rpm) of the rotating antenna. The fractional variation is computed relative to a nominal sample rate* $\boldsymbol{F_s = 25\ Msps}$ *. The trace is one sinusoidal cycle. The maximum effective sample rate is slightly larger than* $\boldsymbol{F_s}$ *when the rotating collector's velocity vector is towards the source (at* $\boldsymbol{\theta_r(t = 0) = 90^\circ}$*) and equal to* $\boldsymbol{F_s}$ *when the rotating collector's velocity vector is orthogonal to the line-of-sight direction of the source (at* $\boldsymbol{\theta_r(t = 5) = 180^\circ}$*).*

As we shall see, this property, which is proportional to the *second* derivative of $\tau_r(t)$ (i.e. proportional to $T\ddot{O}A$), also critically informs the signal processing method.

3.1.2.3 Interval Length:

In Section 3.1.2.1 and Section 3.1.2.2 we have described how, for the high-fidelity simulation of collection, for each point in time t_r on the rotating collector, the appropriate source signal start time is identified (TOA) and the effective sample rate $F_{s,eff}(t)$ determined, the latter being the rate at which the source signal must be resampled to reflect the dilation/compression effects of the rotating collector. The next issue that presents itself is: for what time interval t_{int} can $F_{s,eff}(t)$ be applied before the approximation of a constant sampling rate incurs too much loss of fidelity?

The answer to this question, for collection simulation, involves the time derivative of $F_{s,eff}(t)$, which is implicitly related to the $T\ddot{O}A$ property, that is, the time derivative of $\tau_r(t)$. When we consider Correlation Processing in Section 3.2, we shall see that in that case there is an additional criterion that must be met and that we must therefore examine two effects, or criteria, and choose the value of t_{int} that satisfies the most restrictive of them.

From Figure 8 we can see that the maximum rate of change of $F_{s,eff}(t)$ occurs around $\theta_r = 180^\circ$, and from the figure, the maximum value of $F'_{s,eff}(t) = \partial F_{s,eff}(t)/\partial t$ is $m = -1.612$ samples/s^2. In that angular region, we may express $F_{s,eff}(t)$ with a linear model as

$$F_{s,eff}(t) = F_{s,eff}(t_o) + F'_{s,eff}(t)(t - t_o) = F_{s,eff}(t_o) + m \times (t - t_o)\,, \qquad (12)$$

where m is the slope of the linear function describing the time-variation of $F_{s,eff}(t)$. The task is therefore to determine t_{int} such that:

$$\int_{t_o}^{t_o + t_{int}} F_{s,eff}(t)\partial t - F_{s,eff}(t_o)t_{int} = {}^1\!/_\alpha\,, \qquad (13)$$

where the RHS of Eq. (13) is the amount of sample misregistration we will allow to occur over the interval t_{int} due to approximating a continuously varying sample rate $F_{s,eff}(t)$ by a constant

sample rate $F_{s,eff}(t_o)$. For example, to limit this error to 1/40th of a sample (i.e., $t_s/40$), we choose $\alpha = 40$. Evaluation of Eq. (13) gives

$$\frac{mt_{int}^2}{2} = \frac{1}{\alpha} \text{ , or } t_{int} = \sqrt{\frac{2}{\alpha m}} \ . \tag{14}$$

Based on $m = -1.612$ and $\alpha = 50$, we find $t_{int} \cong 158$ milliseconds. Thus, for the collection process, having determined for time $t = t_r$, associated with rotational position $\theta_r(t_r)$, the effective source-sample rate $F_{s,eff}(t_r)$, we may perform the resampling over an interval of length t_{int} , following which the process is repeated for the next time interval at $t = t_r + t_{int}$, and so on until collection over a half revolution of the rotating antenna is completed.

3.1.2.4 Phase of Collected Signal

For collection an element k of the static boom ULA, designated bk, we have seen (Eq. (2)) that the phase of the collected (baseband) signal is,

$$\phi_{bk}(t) = \phi_{bk} = -\omega\tau_{bk} + \Delta\phi \, . \tag{15}$$

For the *rotating* collection element, the motion which, as we have already discussed creates a dilation/compression effect on the complex envelope of the emitted signal, there is corresponding perturbation on the phase of the RF carrier. This effect is also manifest in the baseband collected signal but it is not automatically imposed onto that signal by the resampling process described in the previous section; instead, it must be imposed numerically based on an analytical model. This effect is generally interpreted as a Doppler shift of the carrier frequency, but for maximum clarity in the following derivation we make recourse to the same quantities we have been using all along. Later, we show that such a derivation is mathematically equivalent to a Doppler shift representation.

For collection interval m starting at time $t = t_{rm}$, the phase of the collected signal, for each sample n taken a rate F_s for the duration (t_{int}) of interval m, wherein $n = 1$ corresponds to time $t = t_{rm}$, is given by

$$\phi_r(n) = -\omega\tau_{r,stat}(n = 1) + \Delta\phi + (n-1)\left(t_{s,eff} - t_s\right)\frac{2\pi}{T_c} \ , \tag{16}$$

where $T_c = 1/f_c$ (s/cycle) is the period of the RF carrier frequency. The third, time-(or sample)-dependent term on the RHS of Eq. (16) reflects the fact that the sampling performed at the receiver of the rotating collector, sampling on intervals of t_s (i.e., at F_s), manifests on the emitted signal waveform, because of dilation/compression effects, as occurring at intervals of $t_{s,eff}$, i.e. at rate $F_{s,eff}(t_{rm})$. To show the equivalence to the Doppler phenomenon, we note that

$$t_{s,eff} - t_s = \frac{\hat{r}_{rs}(t_{rm})\cdot\bar{v}_r(t_{rm})t_s}{c} = \frac{v_{r,rad}(t_{rm})t_s}{c} \, , \tag{17}$$

where $\bar{v}_r(t_{rm})$ is the velocity vector of the rotating collector at time t_{rm} and $v_{r,rad}(t_{rm})$ the radial velocity component of it, that is, the component of it in the direction of the emission source. The quantity $v_{r,rad}(t_{rm})t_s/c$ is thus the very small time increment by which a sample period of the incident signal is altered, in one period t_s of the on-board sampling, due to the radial motion of the collector. Substituting Eq. (17) into the third term of the RHS of Eq. (16), and using $\omega = 2\pi/T_c$ we get

$$\omega(n-1)\left[\frac{v_{r,rad}(t_{rm})t_s}{c}\right] = 2\pi\left[\frac{v_{r,rad}(t_{rm})}{\lambda}\right](n-1)t_s = 2\pi f_d(n-1)t_s\,, \qquad (18)$$

where $\lambda = c/f_c$ is the wavelength of the RF carrier frequency and in which we recognize f_d as the Doppler frequency, that is,

$$f_d = \frac{v_{r,rad}(t_{rm})}{\lambda}. \qquad (19)$$

In terms of Doppler frequency we can therefore alternatively express the phase of the collected signal within interval m (i.e., Eq. (16)) as

$$\phi_r(n) = -\omega\tau_{r,stat}(n=1) + \Delta\phi + 2\pi f_d(n-1)t_s\,. \qquad (20)$$

Finally, equating Eqs. (16) and (20), we find that the effective Doppler frequency f_d for an interval is given by:

$$f_d = \frac{f_c(t_{s,eff}-t_s)}{t_s}\ . \qquad (21)$$

3.2 CORRELATION PROCESSING:

In this section we discuss the signal processing steps employed in correlating the data between, on the one hand, each of the individual static elements bk that comprise the ULA mounted on the rigid boom and, on the other, the rotating collection element, at some position θ_r. Many of the principles utilized closely resemble those described in the exposition given above on collection simulation, but there are also some notable differences. One of these involves the resampling operation that has been discussed above at length. The resampling operation is particularly applicable for *collection* simulation given the known location on the earth of the discrete emission source(s). As we have seen, this information, the exact source location, allows for arbitrarily precise simulation of the collection phenomena. In contrast, with correlation processing we assume that the collected emissions are simultaneously incident from every location within the extent of a distributed source. The correlation processing therefore involves some extra constraints that must be observed.

Fundamentally, the correlation operation, for the rotational position $\theta_r(m)$ and rigid boom antenna element bk, for data segments consisting of N complex samples, is given by

$$\tilde{R}_{bk}(m) = \sum_{n=1}^{N}\tilde{S}_r\,(n)\left[\tilde{S}_{bk}(n)e^{j\omega\Delta\tau}e^{-j\omega_d(n-1)t_s}\right]^*, \qquad (22)$$

where,

$$\Delta\tau = \tau_{bk}\left(t_{bk}(t_r)\right) - \tau_r(t_r)\ , \qquad (23)$$

where $t_{bk}(t_r)$ is the start time of an interval of data captured at element bk, matching the data which was received starting at time t_r at the rotating antenna element, and wherein we assume that the first sample of both of the baseband signals $\tilde{S}_r(n)$ and $\tilde{S}_{bk}(n)$ have been time-aligned. Eq. (22) expresses the adjustments that are made to $\tilde{S}_{bk}(n)$ to phase-match $\tilde{S}_r(n)$, both in fixed phase offset due to the differential propagation path, expressed in Eq. (23), and also in time-dependent phase offset associated with the Doppler shift present for $\tilde{S}_r(n)$. Notably, unlike the collection simulation processing, no resampling of either signal $\tilde{S}_r(n)$ or $\tilde{S}_{bk}(n)$ is performed, representing a significant computational savings. The correlation output values $\tilde{R}_{bk}(m)$

constitute the visibilities that are subsequently applied to spatial basis functions to enable image reconstruction. This latter topic is treated in Section 3.3.

The following sections address the various constraints that the problem geometry and dynamics place on correlation processing and describe how accommodation of these constraints is incorporated into the processing.

3.2.1 Fringewashing and Maximum Extent of Imaging Patch

As discussed above with respect to high-fidelity collection simulation, and which also applies also to correlation processing, due to motion present, time-registration between data streams (rotating collector vs. static elements) must be updated at small temporal intervals. What was *explicit* in the collection concept but which is *implicit* in the correlation process is that this time registration is conducted with respect to a particular location r_o on the earth disk, which for correlation processing corresponds to the center pixel of an image patch on the earth-disk surface.

With R-MXAS, correlation processing, which generates the context-dependent quantities (visibilities) utilized in ultimate image reconstruction, begins with the selection of a location r_o , with respect to which time-registration of the various data streams is accomplished. We consider now the question of constraints on the size of the image patch, centered at r_o for which the derived visibilities are applicable to the image reconstruction. The relevant constraint to consider is based on the principle of *fringewashing*. Fringewashing refers to the decorrelation that occurs in the collection of an emitted signal from a single point of a distributed source, due to the varying propagation distance incurred with its incidence across an extended receiving aperture.

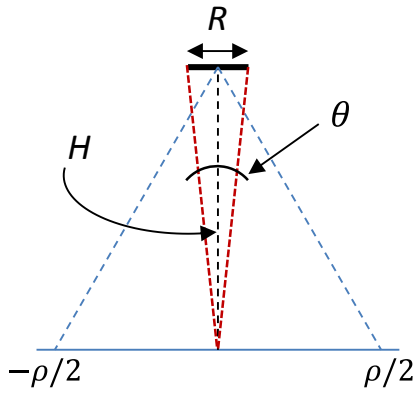

Figure 9: Schematic representation of geometric factors governing the fringewashing effect, for a given bandwidth. *The schematic indicates the maximum allowable ground extent* $\boldsymbol{\rho}$ *that an image patch may have, for a given aperture focus, based on the fringewashing criterion. The figure depicts the applicable geometric parameters, including the aperture extent, the altitude of the aperture, and the angle that the aperture subtends from the ground focus point.*

The geometry of the problem is illustrated in Figure 9**,** showing the angle theta subtended by an aperture of extent $R = 200$ m, located at a height $H = 35800$ km (GEO altitude) above a surface under observation. Assuming the aperture is nadir-focused towards the surface, the maximum extent along the surface away from the nadir point for which emissions can be observed by the aperture, and suffer a correlation loss of $\leq 50\%$ is indicated in Figure 9 by the point ρ. The value of ρ according to the fringewashing criteria is given by ([3, Eq. 30]),

$$\rho = \frac{(c/B)}{2\sin(\theta/2)} \text{ (m)}. \qquad (24)$$

For our simulation scenario, we find $\rho = 2685$ km. However, since this pertains to a 50% correlation loss, and we wish to have a much higher precision level, we choose instead to use $\rho = 500$ km in our processing, corresponding to an image patch having diameter 1000 km. Given that the earth disk from GEO has a diameter of approximately 10,800 km, the number of image patches, N_{spots}, that have to be individually computed, and then combined into one earth-disk mosaic image, is approximately 115.

Having thus determined the maximum image extent based on fringewashing considerations, the next constraint we consider is the maximum time interval t_{int} over which the Doppler shift incurred by the rotating collector can be assumed to be, over the entire extent of that area, constant within some error criteria. As we shall see, computational complexity is greatly mitigated if this assumption can be made for an acceptable value of t_{int}. We have seen in **Section 0** that,

$$f_d(t) \propto F_{s,eff}(t) \propto \mathrm{v}_{r,rad}(t) \ . \tag{25}$$

Thus the question of uniformity of the Doppler shift $f_d(t)$ can be most directly answered by considering the variation of the radial velocity $\mathrm{v}_{r,rad}(t)$ over that area. The maximum value of $\mathrm{v}_{r,rad}(t)$ occurs at (see Figure 6) $\theta_r = 90^\circ$, at which point the entire velocity vector is radial, assuming the image patch is centered in the nadir direction. As illustrated in Figure 10, the fractional variation of the radial velocity over the image area is

$$q = \frac{\mathrm{v}\cos\theta_\rho - \mathrm{v}}{\mathrm{v}} \ , \tag{26}$$

where $\theta_\rho = \tan^{-1}(\rho/H)$ is the angle which is subtended by radius of the image area from the height of the R-MXAS system. For the present scenario, we find $q = 1e^{-4}$. Given this difference in Doppler frequency across the image area, we may now determine the maximum time interval t_{int} for which this Doppler difference would produce a phase error $\Delta\phi$ (degrees), in the correlation operation involving emission from a source element at the very perimeter of this image area.

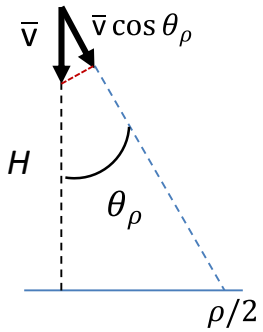

Figure 10: Radial velocity variation over a fringewashing-limited areal extent. *The schematic depicts the relevant geometric quantities governing the variation in radial velocity perceived from a given location on earth, along a line extending from the nadir point, associated with a pure vertically-directed velocity vector at GEO. The angular separation of the two ground locations, from GEO altitude, causes the radial velocity of the non-nadir location to be the projection, by the cosine of the angular extent, of the full velocity vector.*

That is,

$$[f_d - (f_d + qf_d)]t_{int} = \Delta\phi/360 \ , \tag{27}$$

wherein the RHS has been divided by 360 to be in units of cycles of the Doppler frequency. Solving for t_{int} in Eq. (27) gives,

$$t_{int} = \frac{\Delta\phi}{360qf_d} \ . \tag{28}$$

Since, for our scenario, the maximum Doppler shift is $f_d \cong 300$ Hz, then for a maximum phase error of, say, $\Delta\phi = 1^\circ$, we determine that $t_{int} = 69$ ms.

To review our findings to this point, on the topic of correlation processing:

1) To satisfy the fringewashing constraint for an aperture with maximum dimension $R = 200$ m, the imaging of the earth disk should consist of a mosaic of ~115 individually processed images each having an extent (diameter) of 1000 km.

2) For an individual image patch, in treating the data from the rotating collector (details to follow), we can use the approximation that, over an interval of maximum duration $t_{int} = 69$ ms, and incurring a maximum phase error of just $\Delta\phi = 1^{\circ}$, the Doppler frequency corresponding to emission from the very center of the image patch also applies to every other location (pixel) within the image patch.

3) We recall (from Section 0, e.g. Eq. (14)) that for signal resampling purposes, to account for $F'_{s,eff}(t) = \partial F_{s,eff}(t)/\partial t$, the rate of change of the effective sampling rate due to the rotational motion, the maximum interval length should be[1] (Eq. 14) $t_{int} = 158$ ms. Thus the criterion from list item (2) above is more restrictive and therefore sets the interval length.

3.2.2 Correlation Processing without Resampling

There remains one criterion requiring examination. The resampling operation is computationally large relative to the other various operations we have been describing, particularly when it involves a very tiny fractional difference (e.g., $1e^{-7}$, see Figure 8) as occurs for this problem. Implicit in list item (2) above is the notion that one option for correlation processing is to digitally apply a Doppler phase correction, but not resample the complex envelope data itself; this approach is in fact implied in Eq. (22). In such a case, which entirely removes the need for computationally burdensome resampling, the criterion for t_{int} becomes:

$$\left(F_s - F_{s,eff}(t)\right) t_{int} = {}^{1}/_{N_{frac}} \ , \tag{29}$$

where N_{frac} denotes the fractional portion of a sampling interval, t_s/N_{frac}, that, due to the non-equivalent sample rates, the two baseband signals $\tilde{S}_r(n)$ and $\tilde{S}_{bk}(n)$ diverge (become mis-registered) from each other after time t_{int}. We refer to this as a "sample walkoff" phenomenon. The maximum difference metric for the two sample rates, from Figure 8, is $\left[F_{s,eff}(t)/F_s - 1\right]_{Max} \cong 2e^{-7}$. Therefore,

$$\left(F_s - F_{s,eff}(t)\right) t_{int} = F_s \left(1 - \frac{F_{s,eff}}{F_s}\right) t_{int} = F_s(2e^{-7}) t_{int} = {}^{1}/_{N_{frac}} \ , \tag{30}$$

from which,

$$t_{int} = 1/\left[(2e^{-7}) F_s N_{frac}\right], \tag{31}$$

which for, say, $N_{frac} = 40$, yields $t_{int} = 5$ ms. Thus we see that, absent any resampling of the participant signals, the resultant "sample walkoff" effect imposes by far the most restrictive criteria yet seen on the maximum correlation interval length. For the simulation conducted, the results of which we have already referenced in various figures, we used an even shorter correlation interval length of $t_{int} = 2$ ms. Based on this, the number of virtual node locations of that rotating antenna, N_θ, is the number of t_{int} intervals in 10s (i.e., the half revolution time of

[1] As mentioned in Section 3.1.2.3, the actual processing performed for the simulation revealed that $t_{int} \leq$ ~25 ms appeared necessary to obtain sufficient fidelity with the collection processing. It is a topic for further research to understand this departure from the theoretical analysis.

the rotating antenna). Multiplying N_θ by the number of elements comprising the rigid boom ULA, which is for this simulation, 263, gives the total number of visibilities computed, for a single image patch: $(10/2^{-3}) \times 263 = 1{,}315{,}000$. The locations of these visibilities in the u-v plane, as computed in the simulations exercise, are depicted in Figure 4(a).

3.2.3 Aligning Data for Correlation

The correlation expression given in Eq. (22) presupposes that the two data streams, $\tilde{S}_r(n)$ and $\tilde{S}_{bk}(n)$, have been aligned, in terms of their first samples. The explicit process for this alignment is as follows:

1) Starting with the rotating collector, find the sample time t_{rm} (with associated rotational position $\theta_r(t_{rm})$) marking the start of correlation time interval m of duration t_{int}.
2) Use the polynomial expression for $\tau_r(t)$ (see Eq. (5)) to find the time $t_o(t_{rm}) = t_{rm} - \tau_r(t_{rm})$ at which the same sample (signal point) was emitted from the earth surface, assuming an emission source location $\bar{r}_o$, at the center of the current surface area to be imaged.
3) Using the polynomial expression for $\tau_r'(t)$ (associated with Figure 8), compute the effective sample rate $F_{s,eff}(t_{rm})$ applicable to the signal data starting with $\tilde{S}_r(t_{rm})$.
4) Based on $t_o(t_{rm})$, locate the corresponding signal segment $\tilde{S}_{bk}(t_{bk,m})$ at each of the elements of the ULA on the rigid boom, where $t_{bk,m} = t_o(t_{rm}) + \tau_{bk}(t_o(t_{rm}))$ (see Eq. (3)).

As indicated in step (1) above, selection of the $\tilde{S}_r(t)$ data for each time interval t_{int} is engineered to fall on sample boundaries. In general, however, the signal interval start times $t_{bk,m}$ will not fall on sample boundaries for the $\tilde{S}_{bk}(t)$ data. To achieve the required time-registration it is thus necessary to resample the $\tilde{S}_{bk}(t)$ data such that $t_{bk,m}$ falls on a sample boundary. Note that this resampling does not involve changing the sample rate, but is merely a data shift and is efficiently accomplished using the shifting property of the fast Fourier transform (FFT):

$$\tilde{x}(t-\tau) = \widetilde{\mathcal{X}}(f)e^{j2\pi f\tau}, \qquad (32)$$

which formula expresses the fact that a time-shift by time increment τ of a time-domain sequence $\tilde{x}$ is achieved by applying a phase shift to the coefficients $\widetilde{\mathcal{X}}(f)$ yielded by the FFT of $\tilde{x}$. The phase shift is proportional to the product of the time-shift increment τ and frequency f of each coefficient.

3.3 IMAGE RECONSTRUCTION

Given the pronounced out-of-plane baselines engendered in R-MXAS, as well as the non-uniform distribution of those baselines in the u-v plane, the standard approach, FFT-based inversion of the visibilities, is not available for the image reconstruction process. Instead, we employ direct numerical calculation, without approximation, of the spatial basis function associated with each baseline, which spatial basis function is then weighted by the corresponding visibility derived from that baseline. The absolute value of the sum of these weighted baselines, possibly modified by some weighting scheme, accomplishes image reconstruction.

A spatial basis function, for a particular image area (patch) on the earth surface, associated with the baseline between the rotating collector at some angle θ_r and a particular static element bk of the boom-mounted ULA, is given by:

$$\gamma(\theta_r, k, \bar{r}_{pxl}) = exp\left[j\omega\Delta\tau\left(\bar{r}_r(\theta_r), \bar{r}_{bk}, \bar{r}_{pxl}\right)\right], \quad (33)$$

where,

$$\Delta\tau\left(\bar{r}_r(\theta_r), \bar{r}_{bk}, \bar{r}_{pxl}\right) = \tau_\theta\left(\bar{r}_{pxl}\right) - \tau_{bk}\left(\bar{r}_{pxl}\right), \quad (34)$$

where,

$$\tau_\theta\left(\bar{r}_{pxl}\right) = \frac{\left|\bar{r}_r(\theta_r) - \bar{r}_{pxl}\right|}{c}, \quad (35)$$

and,

$$\tau_{bk}\left(\bar{r}_{pxl}\right) = \frac{\left|\bar{r}_{bk} - \bar{r}_{pxl}\right|}{c}, \quad (36)$$

where $\bar{r}_{pxl}$is a pixel location within the image area. Figure 11 shows examples of three different baselines and the associated spatial basis functions for them, computed according to Eq. (33).

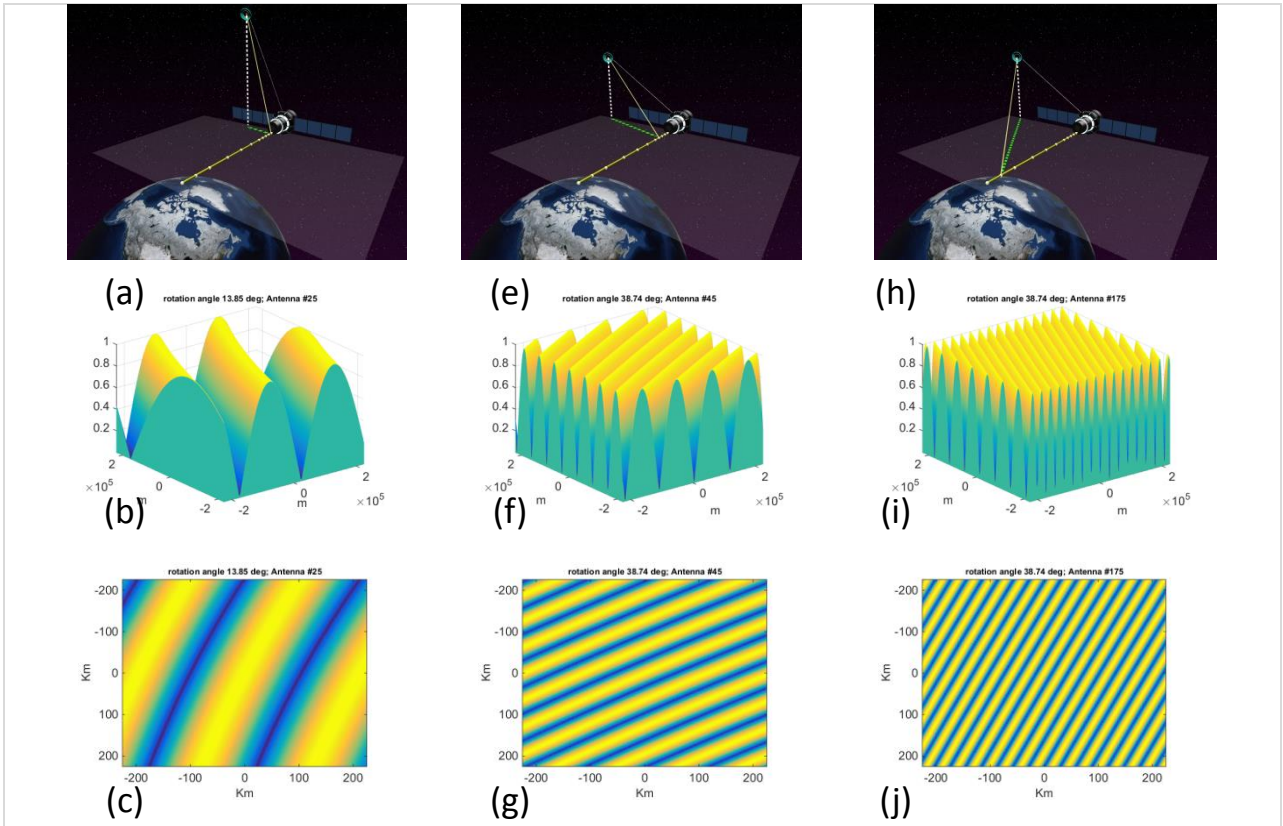

Figure 11: Computed spatial basis functions for three different physical R-MXAS out-of-plane baselines . *The top row, (a)-(c), depicts, using the same rendering of the R-MXAS system as Figure 1, three interferometric baselines, differing markedly in length and orientation, engendered by the R-MXAS system. The middle row, (d)-(f), show in 3-D perspective the quasi-sinusoidal spatial basis functions manifest on the surface of the earth by these baselines, the oscillations differing in period and orientation. The bottom row, shows the same basis functions in a 2D perspective, appearing as alternating yellow and blue stripes over the same 500km x 500km area.*

We now discuss the mathematical implementation of image reconstruction, for a given patch, according to the area-extent limitations discussed in Section 3.2.1. In order to add context pertinent to the dimensions of the various vectors and matrices employed in the implementation,

we first consider the relevant parameters introduced in our sample problem. We consider image reconstruction for a square image patch, the pixels for which are arranged in M rows, each row having M columns. For examples, for the scenario under study, the imaging resolution is 35 km, and the extent of each patch is 1000 km on a side. If we choose to oversample the nominal 35 km PSF by 7x, then we have 5 km pixels, making our image 250 x 250 pixels. We assume for this discussion that the boom-mounted ULA has 300 elements, at that the number of virtual elements created in space over half a revolution by the rotating antenna element is 5000 (i.e. $10\text{s}/t_{int}$, for $t_{int} = 2$ ms).

The mathematical representation of the image reconstruction process is matrix equation shown in Eq. (37).

$$\begin{bmatrix} p_{11} \\ p_{21} \\ \vdots \\ p_{M1} \\ p_{12} \\ \vdots \\ p_{M2} \\ \vdots \\ \vdots \\ p_{M1} \\ \vdots \\ p_{MM} \end{bmatrix} = \begin{bmatrix} \gamma(\theta_r,1,\bar{r}_{11}) & \dots & \gamma(\theta_r,k,\bar{r}_{11}) & \dots & \gamma(\theta_r,N_B,\bar{r}_{11}) \\ \vdots & & & & \\ \gamma(\theta_r,1,\bar{r}_{M1}) & & & & \\ \gamma(\theta_r,1,\bar{r}_{12}) & & & & \\ \vdots & & & & \\ \gamma(\theta_r,1,\bar{r}_{M2}) & \ddots & \ddots & \ddots & \vdots \\ \vdots & & & & \\ \vdots & & & & \\ \gamma(\theta_r,1,\bar{r}_{M1}) & & & & \\ \vdots & & & & \\ \gamma(\theta_r,1,\bar{r}_{MM}) & \dots & \gamma(\theta_r,k,\bar{r}_{MM}) & \dots & \gamma(\theta_r,N_B,\bar{r}_{MM}) \end{bmatrix} \begin{bmatrix} \tilde{R}_1(\theta_r) \\ \tilde{R}_2(\theta_r) \\ \vdots \\ \tilde{R}_k(\theta_r) \\ \vdots \\ \tilde{R}_{N_B}(\theta_r) \end{bmatrix}, \quad (37)$$

$(N_{pxl} \times 1)$ $(N_{pxl} \times N_B)$ $(N_B \times 1)$

which we may express as,

$$\bar{p}(\theta_r) = \bar{\Gamma}(\theta_r)\bar{v}(\theta_r)\,, \quad (38)$$

wherein the LHS vector $\bar{p}(\theta_r)$ contains the complex values of the pixels of an intermediate- or sub-image product produced by the visibility-weighted baselines obtained from one rotational position, θ_r , associated individually with each of the N_B antenna elements of the boom-mounted ULA. To form the complete image, the LHS vector $\bar{p}(\theta_r)$ is accumulated for all of the different θ_r positions. The total number of pixels in the imaging area is $N_{pxl} = M \times M$, and the 2D pixel map is organized for representation in vector $\bar{p}(\theta_r)$ in stacked column order; that is, the first M elements of $\bar{p}(\theta_r)$ correspond to the first column of the image grid. Similarly, the k^{th} column of the matrix $\bar{\Gamma}(\theta_r)$ contains, in the same column-stacked format, the full 2D basis function associated with a single baseline between element bk and the virtual node associated with the rotating antenna at its position θ_r. These are the basis functions depicted, for example, in Figure 11. Finally, the visibility vector $\bar{v}(\theta_r)$ contains the N_B (e.g. 300) visibilities, one for each element of the ULA, for the current rotational position θ_r, computed according to Eq. (22) for data spanning a time interval t_{int} .

Inspection of Eq. (37), and the form of the spatial basis functions given in Eq. (33), suggests methods for efficient implementation. Considering Eqs. (33)-(36), a representation of $\bar{\Gamma}(\theta_r)$ is,

$$\bar{\Gamma}(\theta_r) = exp\left[-j\omega\left(\bar{D}_b - \bar{d}_r(\theta_r)\right)/c\right], \quad (39)$$

where the elements of matrix $\bar{D}_b$ and vector $\bar{d}_r(\theta_r)$ are simply distances, from the various collection nodes---the ULA elements in the former case and the particular angular position θ_r of the rotating antenna in the latter---to each pixel location $\bar{r}_{pxl}$ in the imaging area (patch). In particular $\bar{D}_b(:,k)$, the k[th] column of $\bar{D}_b$, is the distance from element bk to every pixel in the 2D image grid, those values stacked by column order into a single column. Similarly, $\bar{d}_r(\theta_r)$ is a vector containing the distances to every pixel from the rotating antenna position θ_r, also arranged in stacked-column order. We also note that in Eq. (39) we assume that the subtraction of the vector $\bar{d}_r(\theta_r)$ from $\bar{D}_b$ is performed with singleton expansion enabled, i.e., the subtraction is applied to each column of $\bar{D}_b$.

Based on the form of Eq. (39), we can see that, in the ideal state of a completely static rigid boom over the image formation period (e.g. 10s), matrix $\bar{D}_b$ needs to be computed only once and the output sub-images associated with each of the rotational positions θ_r accumulated in vector $\bar{p}(\theta_r)$, as

$$\bar{p}_i = \left[\left|\left(\sum_{n=1}^{N_\theta} exp\left\{j\omega\left(\bar{D}_b - \bar{d}_r(n)\right)/c\right\}\right)_i\right|\right], \tag{40}$$

in which we have denote by the vector designation $\bar{p}_i$ that this complete image result is the magnitude of the sum of the weighted baselines, as indicated by the RHS notation which is intended to denote element-wise absolute value of the vector. Absent from Eq. (40) are any additional weighting coefficients that might be applied to improve the imaging quality. The result of the application of Eq. (40), in which case a Blackman weighting function has also been applied, is shown in Figure 4(c), and illustrates the imaging performance of R-MXAS, in terms of a PSF. Figure 5 compares the principal cuts of the PSF with and without the Blackman weighting function.

3.4 Computational Size Assessment and Preliminary Implementation Concept for Processing

Based on the nominal parameters of the R-MXAS system and intended operational scenario, we can size the various mathematical quantities introduced in the preceding section. We first note that, as discussed earlier, the notional size of the image patch is $N_{pxl} = M \times M = (250)^2 = 62{,}500$. The number of elements comprising the ULA is $N_B = 263$. The number of discrete rotational positions, based on $t_{int} = 2$ ms, is $N_\theta = 5000$. Also, as noted in Section 3.2.1, given the maximum extent of an image patch, full earth-disk imaging requires $N_{spots} = 115$ separate iterations of correlation processing and image reconstruction. Based on these, for a single image patch we have:

- Image values vector $\bar{p}_i$ is $N_{pxl} \times 1 \Longrightarrow 62{,}500$ elements.
- Distance matrix, $\bar{D}_b$, is $N_{pxl} \times N_B \Longrightarrow 16{,}437{,}500$ elements
- Visibility vector for one rotational position, $\bar{v}(\theta_r)$ is $N_B \times 1 \Longrightarrow 263$ elements
- Total number of computed visibilities, $N_B \times N_\theta \Longrightarrow 1{,}315{,}000$

When these various entities are multiplied by N_{spots}, they become relatively large. For example, computation of distance matrix, $\bar{D}_b$, for the all of the image patches involves $1.89e^9$ total calculated distances, and computation of $N_B \times N_\theta \times N_{spots} \Longrightarrow 151e^6$ visibilities. Furthermore, based on the description provided in Section 3.2, the correlation processing does not admit the use of real-time streaming correlators, but is instead an algorithm which must be

carried out on digitally-sampled data, an algorithm involving evaluation of polynomials to retrieve parameters and various operations with those parameters such as Doppler correction. The polynomials themselves are derived using the position measurement data that is contemporaneous with the data being processed.

Notwithstanding the computational size of the correlation processing effort, it is almost certainly necessary to carry out the correlation processing on-board. The total data volume from $N_B + 2$ collectors (which number includes the rotating collectors), all continuously digitizing data at a nominal complex sampling rate of $F_s = 25$ Msps, is roughly 6.623 Gsps, much too large to be downlinked to a ground station. In contrast, as mentioned above, performing the correlation processing on-board results in ~151 million complex values produced every half-revolution, 10s for the current example. Depending on the dynamic range of the visibility data and consequent precision requirements, downlink of such a data volume may be readily accommodated using a downlink rate of a few hundred Mbps.

A design trade that presents itself based on this analysis is using a much slower revolution rate than what was chosen (3 rpm) for this simulation and analysis. Given that for the target application the integration time is expected to be on the order of two hours (see Table 1), it is unnecessary to have a 10s effective image update rate, i.e. the time of one half revolution. If instead the rotation rate is greatly slowed, then the time interval over which the visibility data is computed, and hence the time interval over which the same ~151 million visibility values must be downlinked, is greatly extended, and hence the downlink capacity requirements greatly reduced. The tradeoff that will need to be studied is the increased computational complexity of the proportionately larger volume of data that will be correlated in each time interval t_{int}, which latter parameter will itself become larger inversely proportional to the change in revolution rate.

4.0 ADDITIONAL INNOVATIONS FROM PHASE I RESEARCH

4.1 ANTENNA ARRAY SPARSITY

The ability to impart additional sparsity to the rigid boom ULA was a major Phase I goal. In its "basic" implementation, of a fully-populated ULA and a single (on each end) rotating antenna, R-MXAS affords an antenna reduction relative to the SOTA Y-design of 2X, which, while valuable, might not justify development of such a highly unconventional system. Furthermore, it was determined in the course of the study that the original premise of using standard Low Redundancy Linear Array (LRLA) methods (e.g. [4]) implemented on the rigid boom is not a valid approach. Since R-MXAS is a "Principal Solution" approach in which baselines are formed strictly and non-redundantly between each ULA antenna and the rotating antenna, an LRLA implementation provides no mechanism by which replacement occurs for the baselines formerly formed between the rotating antenna and the now "missing" antennas.

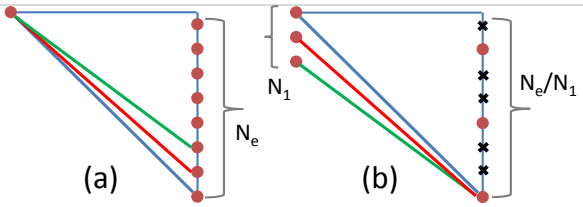

Figure 12: Interleave / decimate concept for achieving antenna sparsity in R-MXAS. *Side-by-side figures illustrate that geometrically-identical baselines (length and orientation) are produced by two configurations: a) a single tether-end antenna and a boom-mounted fully-populated ULA; and b) a small tether-end array of N_1 antennas and a boom-mounted ULA decimated by N_1.*

Fortunately, a major insight from the Phase I research, depicted as a detail in Figure 1 and functionally illustrated in Figure 12, is that the same set of baselines is created, and hence the same aperture, by using a small linear array of N_1 antenna elements at the end of the rotating

tether (instead of a single element, which was the original concept), and simultaneously decimating the full uniform linear array (ULA), originally consisting of N_e antennas, by the factor N_1. With this interleaving / decimation principle it can be shown that the minimum total number of antennas is achieved when $N_1 = \sqrt{N_e}$, making the total number of antennas $N_e' = 2\sqrt{N_e}$. For example for a Y-design with $N_{eY} = 1800$, a basic implementation of R-MXAS would need $N_e = 900$, but a maximally sparse R-MXAS design requires just $N_e' = 60$ antennas, a SWaP reduction, in terms of antennas relative to the Y-design, of 30X. We note that this approach to sparsity has been described previously for 1-D arrays [5], but to our knowledge, it is completely novel to a 2-D array, and especially in the present context of motion and consequent temporal distribution of baseline realization. An additional benefit of the decimated array is the practical elimination of mutual coupling effects due to widely-space antennas.

4.2 RADIOMETRIC SENSITIVITY

Radiometric Sensitivity is a critical consideration for practical implementation of a large, highly sparse SAIR. It is an inescapable law of physics that sparsity engenders reduced radiometric sensitivity. A major theme associated with the R-MXAS concept is the notion of trading unprecedented sparsity for integration time, for applications where such a trade is acceptable. Reduced radiometric sensitivity can all too easily lead however to untenable integration time requirements. One innovation for significantly enhancing R-MXAS sensitivity is the use of a *redundancy linear array*: additional antennas at tether end, arrayed in the rotational plane and maintained (the linear array) in a horizontal attitude (i.e. despun). We recall that the previously described tether-end linear antenna array, utilized for enabling high sparsity of the ULA through an interleave / decimation principle (e.g. Figure 12) is oriented *parallel* to the rigid boom, and thus orthogonal to both the plane of rotation and also to this redundancy array. Thus the architectural manifestation of incorporation of both types of linear arrays is a 2-D array, for example 3x3, at the tether end. The function and value of the *redundancy* dimension of this array is that it allows reproduction of the exact same set of baselines, at very slightly different rotational angles (and hence slightly different times), as illustrated in Figure 13. Such a redundancy in baselines has been shown to have great importance in enhancing radiometric sensitivity, and its use in R-MXAS can be shown (see, e.g. **Table 1** in Section 5.1) to help enable feasible integration times for sparse designs. In an inexact analogy, this approach resembles time-delay integration (TDI), a common method of sensitivity enhancement used in optical imaging with charge-coupled devices (CCDs).

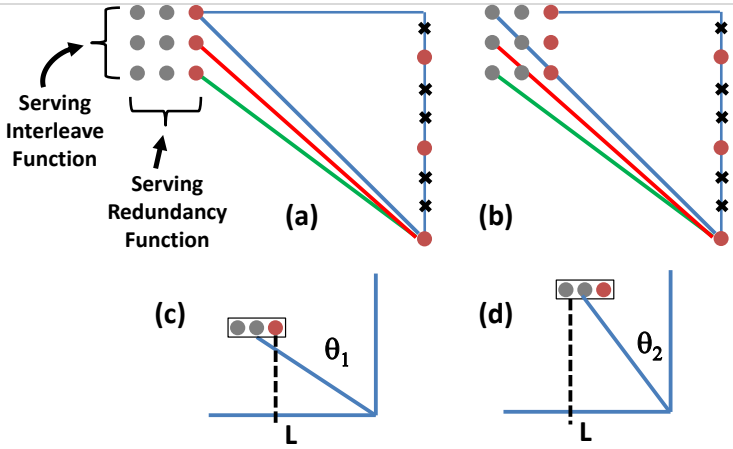

Figure 13: Method for baseline redundancy based on tether-end array dimensionality orthogonal to the rigid-boom. *Side-by-side line schematics illustrate that such a tether end array dimension causes reproduction of the same projected baseline, L, at slightly different rotational positions: (a)-(b), top view for two different rotational positions; (c)-(d) side view for the same two rotational positions.*

An alternate exploitation angle regarding a tether-end 2D array, which represents a particularly exciting aspect to investigate in Phase II, is the use of this 2D array as a single large aperture, in the form of a phased array. Such an approach could potentially have a dramatic impact on sensitivity. We know that integration time τ_{int} is a very sensitive function of antenna dimension d, namely, $\tau_{int} \propto d^4$. Thus the idea of having, as one of the participant antennas of *each* interferometer, a very large aperture (the phase array) could potentially afford a profound improvement in the radiometric sensitivity of sparse arrays. Among the operational implications of such an approach is that the relatively narrow beam of a large phased array antenna would cover a much smaller angular region than the individual antennas on the ULA. Thus, for an R-MXAS implementation, a concept of operations would need to be defined whereby the phased array focuses in a slightly different direction on each successive revolution of the antenna, or else is operated as an *N*-channel array, in which the signal from each element antenna of the array is separately digitized, instead of all analog combined, so that for the same data collection, focusing could be performed across all applicable angular directions, effectively comprising all of the area contained within the footprint of any one of the individual ULA antenna's beam. It is interesting to note that such an idea is available only to R-MXAS, relative to all other SAIR approaches, because only R-MXAS (to Leidos' knowledge) has the property (or can have the property) of having one particular antenna as participant in every interferometric baseline formed. As such, this aspect for future investigation has the potential of introducing a sensitivity enhancing effect that would greatly expand the applicability of highly sparse designs.

5.0 COMPARISON WITH OTHER CONCEPTS

5.1 GEO-BASED SMOS MISSION: R-MXAS VS. Y-DESIGN

Table 1 illustrates the impact of an R-MXAS design relative to the design parameters that would accompany a GEO-based SMOS mission based on the Y-design depicted in Figure 3**.** The approach taken is to scale up the legacy LEO SMOS L-SMOS design to a GEO altitude, which design we term G-SMOS, in such a way as to preserve spatial resolution (at ~35 km) and radiometric sensitivity. Then we design an R-MXAS system that will yield the same spatial resolution, and determine what integration time would be required for it to similarly achieve the same radiometric sensitivity as the Y-designs, in GEO and LEO, respectively. Our radiometric sensitivity analysis is based on equating the SNR per pixel, relative to the legacy L-SMOS design. Thus for all three systems, we assume the receiver noise power to be the same, $P_N = FkT_{REC}B$, where F is receiver noise figure, k is Boltzmann's constant, T_{REC} is the receiver equivalent noise temperature and B the receiver bandwidth. SNR being defined as P_R/P_N, the approach is to apply the various factors by which the received power, P_R, for both the G-SMOS and R-MXAS designs, is altered relative to L-SMOS, and then determine the integration time by which the SNR for the new designs is made equal to L-SMOS. Thus for G-SMOS, the relevant factors modifying the received power, relative to L-SMOS are as follows.

Distance Loss Ratio, L_R: The power density incident upon G-SMOS is modified relative to L-SMOS by the square of the distance ratio. Using 35,800 km for GEO and 900 km for the nominal L-SMOS slant range (i.e. 760 km altitude with a 32^o tilt), we have:

$$L_R = \left(\frac{900}{35800}\right)^2 \cong \frac{1}{40^2} \ . \qquad (41)$$

***Antenna number ratio, L_{Ne}*:** To achieve the same angular resolution, the three 4-m arms of L-SMOS have to be lengthened by the distance ratio, which as we have seen is ~40X. The L-

SMOS antenna *spacing*, however, which is 0.875λ, can be relaxed at GEO by a factor of 4X to 3.5λ without incurring aliasing from grating lobe effects, a consequence of the fact that the earth disk subtends an angle of only 17.4° from GEO altitude. Thus the antenna number ratio for G-SMOS relative to L-SMOS is,

$$L_{Ne} = \frac{40}{4} = 10\,. \tag{42}$$

Antenna element aperture ratio, R_{Ap}: In addition to being spaced 4X further apart, the individual antenna element size of the antennas for G-SMOS can be 4X larger than for L-SMOS, increasing power intercept and hence total received power. At the larger size, the main beam of the antenna element is still large enough to span the angular extent of the earth disk from a GEO altitude. The aperture is proportional to the square of the antenna dimension, hence,

$$R_{Ap} = 4^2 = 16. \tag{43}$$

Ratio of integration times, $R_{\tau G}$: The final factor affecting relative SNR is the square root of the integration time. Currently for the L-SMOS operational mission $\tau_L = 1.2$ s. Thus,

$$R_{\tau G} = \sqrt{\frac{\tau_G}{\tau_L}} = \sqrt{\frac{\tau_G}{1.2}}\,. \tag{44}$$

Given these modifying parameters, we have that,

$$SNR_G = SNR_L \times L_R \times L_{Ne} \times R_{Ap} \times R_{\tau G}\,, \tag{45}$$

from which we determine the G-SMOS integration time necessary to cause $SNR_G = SNR_L$:

$$\tau_G = {1.2}\Big/{\left(L_R \times L_{Ne} \times R_{Ap}\right)^2} = 120\text{ s}\,. \tag{46}$$

Thus, the G-SMOS design with equivalent radiometric sensitivity to (L-)SMOS uses 690 antennas, each 4X larger than for L-SMOS and spaced 4X further apart, and requires an integration time of 120 seconds versus 1.2 seconds for L-SMOS.

Similarly for the R-MXAS design, we have employed the fact that the basic R-MXAS design requires (see Section 4.1) half as many antennas as the G-SMOS Y-design, therefore, 345 elements. However, we additionally exploit the sparsity measure outlined in Section 4.1, adding a small array of five antennas at tether end and decimating the rigid boom ULA by the same factor (five). Further we use four tether arms spaced at 90 degrees to reduce the full aperture creation time τ_{image} down to one quarter revolution, which, for 3 rpm becomes $\tau_{image} = 5$ seconds. Finally, exploiting the innovation described in Section 4.2, we include a redundancy dimension to the tether-end array, of rank four. The final design is summarized in Table 1. There are thus $(345/5) + 4 \times (5 \times 4) = 149$ total antennas in the R-MXAS design. For our SNR calculation however, we consider that the redundancy dimension of the tether-end array is not explicitly associated with the creation of the same full aperture in one quarter revolution, but rather enables four (in this case) redundant full apertures to be created in the same time τ_{image}. Hence, for our antenna number ratio, $L_{Ne,RMX}$, we omit the elements associated with the aperture redundancy, as

$$L_{Ne,RMX} = \frac{({}^{345}/_{5}) + (4\times5)}{69} = \frac{89}{69} = 1.29\,. \tag{47}$$

The redundancy is captured in an additional modifying parameter, $N_{Red} = \sqrt{4}$. Finally, to accommodate the temporally-distributed full aperture creation process in R-MXAS, in contrast to the instantaneously-collected aperture for the SMOS designs, we require that the effective integration time for R-MXAS be understood as effective integration time of the full aperture, and we therefore define the ratio of integration time, $R_{\tau RMX}$, of R-MXAS relative to L-SMOS, as,

$$R_{\tau RMX} = \sqrt{\frac{\left(\tau_{RMX}/\tau_{image}\right)}{\tau_L}}. \tag{48}$$

The modification factors that relate the R-MXAS SNR, SNR_{RMX}, to SNR_L are summarized therefore as:

$$SNR_{RMX} = SNR_L \times L_R \times L_{Ne,RMX} \times N_{Red} \times R_{Ap} \times R_{\tau RMX} \ , \tag{49}$$

from which we determine the R-MXAS integration time, τ_{RMX} , necessary to cause $SNR_{RMX} = SNR_L$:

$$\tau_{RMX} = \frac{\left(\tau_L \times \tau_{image}\right)}{\left(L_R \times L_{Ne,RMX} \times N_{Red} \times R_{Ap}\right)^2} = 9013.9 \text{ s} = \ 2.5 \text{ hrs}\,. \tag{50}$$

Thus, the R-MXAS design with equivalent radiometric sensitivity to L-SMOS uses 149 antennas, each 4X larger than for L-SMOS and spaced 4X further apart, and requires an integration time of 2.5 hours versus 1.2 seconds for L-SMOS.

Table 1: Comparison of SMOS and R-MXAS Designs for a GEO Orbit-based SMOS Mission

Attribute	L-SMOS	G-SMOS	R-MXAS	R-MXAS Details
#Antennas	69	690	149	• Rigid boom is a nominal 345 element ULA, reduced to 69 elements by 5X decimation • Four tethered "spokes" at 90-degree increments, each with a 5x4 array, rotated at 3rpm • Tether-end array: Row dimension (5 elements) interleaves with the decimated ULA to provide all baselines; column dimension provides 4X baseline redundancy for increased sensitivity.
Integration Time	1.2s	2 mins	2.5 hrs	
Structure	3 4-m arms	3 160-m arms	240-m rigid boom and tether radius	

It is interesting to note from **Table 1** that the G-SMOS implementation affords a measurement rate, 2 minutes, which is much more rapid than needed to serve science purposes, for a slowly-varying parameter like soil moisture. There is, however, no "reduced" implementation of a Y-design sparse array possible that would still afford the required spatial resolution (35-km). In contrast, R-MXAS *decouples* the spatial resolution and radiometric sensitivity system requirements. The 35-km spatial resolution requirement can be met with a R-MXAS design having just 37 (i.e. $2\sqrt{(690/2)}$) antennas; however, this leads to an unacceptably long integration time requirement. Similarly, additional antennas could be added to further reduce the integration time. The 2.5 hour integration time represents a reasonable measurement refresh rate for the parameter of interest, while still affording a significant, nearly 5X reduction in antenna SWaP.

5.2 COMPARISON TO OTHER LEADING INNOVATIONS IN LARGE RF APERTURE SYNTHESIS

R-MXAS has significant advantages relative to previously studied work. We have already discussed at length the advantages of R-MXAS over the SOTA Y-design. Two other recent concepts, which have been the subject of significant R&D, including major prototypes, are Clock Scan (CS) ([6,7]) and Geostationary Interferometric Microwave Sounder (GIMS) ([8,9]). The CS concept involves, in the most basic version, two booms of slightly different lengths rotating at slightly different rates in the same plane. The booms have either single antennas or linear arrays (the latter oriented in the circumferential dimension) at each end. Rotational parameters may be selected by which, over multiple/many revolutions, the baselines formed from the various boom-end antennas create a well-sampled u-v plane and hence a SAIR. CS thus uses a very small number of antennas—in the limit, just two. The radiometric sensitivity is very low since each baseline, like R-MXAS, has a very small integration time, due to the motion, but also, unlike R-MXAS, the aperture creation process is very inefficient, requiring many revolutions, whereas R-MXAS requires only ½ or ¼ revolutions, dependent on its configuration. R-MXAS therefore benefits from the sensitivity-enhancing measure of aperture averaging, many times over, in the time it takes CS to synthesize a single aperture.

GIMS employs a sparse array design arranged around the perimeter of a rotating (in the plane of the SAIR, around its own axis) circular structure having the diameter of the desired SAIR. In principle, it is equivalent to rotating a LRLA, which process is readily understood as producing a fully populated u-v distribution within the design extent. The GIMS researchers have determined that a circularly-arranged element pattern can increase the level of sparsity relative to the LRLA. Unlike CS, and like R-MXAS, GIMS creates a full aperture in ¼ revolutions of the entire structure. The maximum sparsity level that GIMS can achieve appears to be slightly worse than for R-MXAS, but it is comparable. The two principal disadvantages of GIMS relative to R-MXAS, both relating to R-MXAS features described in Section 4.0, are the following: 1) Unlike the redundancy array concept described for R-MXAS, there is no obvious method by which GIMS can achieve wholesale redundancy of baseline creation short of reproducing the entire sparse array, slightly offset from its original version, which is costly in terms of element numbers; and 2) since GIMS exploits the combinatorics of its physical array to create, at any moment, a large collection of baselines, there is not a feasible technical path to a measure like that described for R-MXAS in which one high-gain antenna could be used to dramatically boost the radiometric sensitivity of the concept.

A final disadvantage of both GIMS and CS relative to R-MXAS is that since in both concepts all of the antennas rotate in the aperture plane, and thus continuously change their collection polarization, complex measures are required to synthesize an aperture at a single polarization.

6.0 TECHNOLOGY IMPACT: POTENTIAL NEW MISSIONS AND/OR CAPABILITIES AFFORDED TO NASA AND THE GREATER AEROSPACE COMMUNITY

6.1 POTENTIAL NEW MISSIONS AND / OR CAPABILITY LEAPS ENABLED

In the 2015 NASA Technology Roadmap, the goal of developing larger collecting apertures with better performance and less mass is the primary goal (termed “Sub-Goal”) for Technology Area 8.2, *Science Instruments, Observatories, and Sensor Systems: Observatories*. A decomposition of the TA-8.2 Sub-Goal calls out, as one of three specific technologies required to meet the needs of planned and potential future NASA missions, the concept of Distributed Aperture, that is, methods to create an extra-large aperture via deployment, assembly, or

formation flying—where formation flying technology is an actively controlled *virtual* structure. A key application area noted (one of three) supported by this technology is microwave antennas for earth science. R-MXAS represents an innovative approach, warranting further research, to meeting and/or exceeding this set of goals envisioned in the Technology Roadmap.

This need for innovation to increase aperture size (e.g. "5 to 10-fold") for use in conjunction with space-based RF sounders and imagers has been designated as a priority by the earth science community for its importance in informing critical weather and climate understanding. This is reflected in the 2007 *Decadal Survey for Earth Science and Applications from Space* (ESAS), conducted by the National Research Council, an arm of the U.S. National Academies of Science; in the recent compilation of white papers [10] submitted by the ESAS community in support of the *2017* decadal survey, currently underway; and in a 2016 microwave remote sensing investment strategy update reported ([11]) by the NASA Earth Sciences Technology Office (ESTO). As an aerospace architecture, R-MXAS has the potential to provide significant benefits to NASA in the following ways:

1) ***Enhanced capabilities for existing missions*:** A clear desire from the science community, expressed emphatically at the aforementioned IGARSS conference, is for higher resolution (e.g. 5 – 10 km vs. 35-km) SM mapping from space. This problem is daunting mostly due to the increased requirement for radiometric sensitivity since a, say, 5-km "pixel" emits 49X weaker specific intensity than does a 35-km pixel. This leads to an undesirable trade options between an untenable number of antennas or an infeasibly long integration time. The idea (Section ?) of a tether-end 2-D array acting as a high-gain phased array, a participant of every baseline formed, could be the game changer that enables such challenging missions.
2) ***Alternative implementation paths for planned missions*:** As a variation of the analysis done above for a GEO SMOS mission, for the same number of deployed antennas, and same refresh rate, a larger effective aperture and hence finer spatial resolution could be realized for the planned GeoSTAR mission ([12,13]).
3) ***New missions currently considered infeasible owing to the scale involved*.** Examples include: 1) the GEO-based SMOS (L-band) mission described above; and 2) a polar solar orbit imager for interplanetary Coronal Mass Ejections (ICMEs), to inform understanding of solar-earth space weather and its impact on deep space missions to include travel to Mars. As 150 MHz has been identified ([14]) as the key sensing frequency in that application, the question of feasible aperture size becomes critical.

For the greater aerospace community, successful development of R-MXAS provides a compelling technology approach for any sensing application which would benefit from a large virtual array with low SWaP-C. One such example is high-sensitivity, precision geolocation of discrete RF emitters, from a single platform, including for such missions as search and rescue, i.e., geolocating a beacon. Made large enough and located in GEO, such a system could serve its function in a synoptic fashion, at least over the disk of the earth facing it. In fact, this is arguably an excellent example of an application in which the spatial resolution attribute of an aperture is far more important than the sensitivity, given that the sources of interest may not be particularly weak, making their geolocation a perfect candidate application for extremely sparse designs.

6.2 NASA / AEROSPACE COMMUNITY INTEREST / ADVOCACY FOR R-MXAS

One of the most prominent topics during last year's (2018) IEEE International Geoscience and Remote Sensing Symposium (IGARSS), the subject of many sessions and dozens of presentations, was the global SM mapping mission, in terms of ESA SMOS and NASA Soil

Moisture Active Passive (SMAP) mission status, and also in terms of future technology needs. In particular, NASA GSFC scientists closely associated with the SMAP program presented a talk entitled "Determination of the Best Microwave Antenna Approach for Future High Resolution Measurements from Space – An Architecture Trade Study" which outlined the somewhat daunting challenges and called attention to the fact that "advances in technology leading to larger effective aperture size will be needed to meet future resolution requirements." Evidence of enthusiasm by the geoscience and aerospace community in at least the *theoretical underpinnings* of R-MXAS, is that the articles ([3,15,16]) describing these underpinnings, written by R-MXAS PI Dr. John Kendra, and published in *IEEE Transactions on Geoscience and Remote Sensing* were awarded the 2018 IGARSS Transactions Prize Paper Award, which recognizes the paper judged most exceptional in terms of content and impact on the Geoscience & Remote Sensing society, from among all those published in 2017 in the aforementioned journal.

Notwithstanding the aerospace community's interest in large RF apertures in space, R-MXAS, especially prior to the release of the Phase I Final Report, is likely regarded as not only extremely novel in concept, but also, possibly, even anathema to a set of principles, which we might term conventional SAIR, which have been painstakingly established over a decades-long collective effort by many distinguished researchers across the world. In the outreach and communications Leidos made during Phase I to members of the aerospace community highly-qualified in the SAIR domain, including at the aforementioned IGARSS conference, a clear message was that the out-of-plane baselines aspect in particular was problematic, possibly even fatal, to the concept. As was detailed in Sections 2.0 and 3.0, the Phase I effort has yielded resounding evidence illustrating the validity of such an approach, and also the feasibility of the computational effort. Leidos is confident that with these results, and bolstered by additional engineering analysis focused on practical implementation, R-MXAS will begin to gain advocacy as an enabling space technology.

7.0 PLAN FOR FUTURE WORK

The Phase I R-MXAS investigation consisted exclusively of analysis, modelling, and simulation (M&S) to answer some very fundamental questions concerning the concept validity and feasibility. Those questions, as evidenced in the proceeding discussion, have been convincingly answered in the affirmative. Novel and sophisticated signal processing methods lie at the heart of the R-MXAS concept, and future work must include refinement of those methods, as well as investigation of some critical outstanding aspects. The second major task of a future work plan is a comprehensive engineering analysis of the R-MXAS architecture. This analysis will focus on the key feasibility challenges to implementation, and investigate the technology solutions that might meet those challenges. These two major tasks, the SAIR signal processing development and engineering analysis, should proceed in a complementary fashion, with the former serving to determine physical requirements for successful performance of the method, and the latter determining the engineering solutions by which the requirements may be met. The culmination of this effort will thus be a technology development roadmap sufficient to inform decisions of how or whether to continue R-MXAS system development.

The following sections provide additional detail on the specific sub-tasks that would be undertaken for these two major areas of investigation of a future work plan.

7.1 SIGNAL PROCESSING DEVELOPMENT

The signal processing development effort is concentrated in three primary sub-tasks:

1) ***Sensitivity analysis:*** This sub-task will examine, through analysis and M&S, the sensitivity of R-MXAS performance, in terms of imaging quality, to perturbations / errors in time, frequency, and phase registration, and position knowledge; findings will feed the engineering analysis.
2) ***Processing architecture:*** As has been noted, R-MXAS involves signal processing measures that are significantly more complex than utilized in conventional SAIR method. For example, conventional SAIR implementations utilize banks of real-time correlators to which the collected digitized signal from each antenna + receiver are streamed for pairwise combination with the data from (most) every other antenna. Due to the rotational motion involved, the R-MXAS correlation processing involves multiple steps that are executed on very short time intervals, a process traceable to the time-varying aspect of the rotating antennas. A detailed description of the process was presented in Section 3.0. Simply put, the correlation between the rotating antenna data and any of the static antenna's data requires computation and then application of factors associated with the concepts of time-of-arrival, or TOA , and its first and second derivatives, commonly expressed as $\dot{TOA}$, ("TOA-dot") and $\ddot{TOA}$ ("TOA-double-dot"), which concepts are closely related to Doppler frequency and the rate of change of Doppler frequency, respectively. The sub-task will investigate the overall processing architecture, and in particular the allocation of processing on-board vs. on the ground, and associated implications for SWaP-C, latency, and downlink capacity.
3) ***Further innovations:*** The Section 0 discussion identified multiple innovations in the R-MXAS architecture directly affecting the sparsity and also the radiometric sensitivity. As discussed, most of these innovations manifest in the architecture as a tether-end 2-D array. This sub-task explores the efficacy of these measures. A particular emphasis is the validity / feasibility of using a relatively large tether-end 2-D array in the capacity of a single high-gain aperture (phased array) to provide potential groundbreaking sensitivity amplification for a highly sparse array.

7.2 ENGINEERING ANALYSIS

In the development of a future work plan for this report, Leidos has consulted with Atmospheric & Space Technology Research Associates (ASTRA), who have extensive experience in developing innovative scientific systems and fielding them into space. The following analysis represents ASTRA's preliminary assessment of a development plan for R-MXAS.

Orbiting at GEO, the R-MXAS spacecraft conceptual design consists of a series of very long baseline deployable structures with RF sensors applied at specific points of the structures (see Figure 14**)**. One of the deployed structures consists of a ~240 m stationary segment directed away from the spacecraft (parallel to the spacecraft long axis), holding an array of nadir-pointed RF sensors. The second structure consists of two approximately ~240 m booms, centered on the spacecraft, rotating at a rate (ω_1) of one

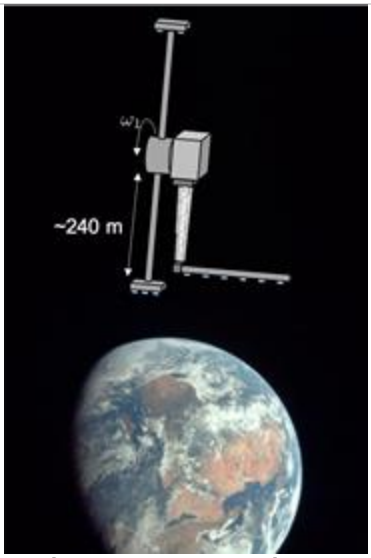

Figure 14: R-MXAS boom deployment conceptual design. *A realistic drawing of an R-MXAS system above the earth. The rotation hub is raised above the rigid boom ULA such that, at its lowest point, the tether-end antenna array is at the same altitude as the rigid boom. The "tether" is itself depicted as a rigid boom.*

rotation per minute, with RF sensors located at the tips of each boom. ASTRA's preliminary assessment is that rigid rotating booms are more feasible than the previously proposed cable tethers since they will be easier to control when performing maneuvers. The extremely large aperture that R-MXAS delivers will enable game-changing science, but introduces numerous technical challenges. ASTRA has identified the following as key technical challenges that are unique to implementation of R-MXAS:

- Design and stowage of the deployables (e.g., required volume and stowing process)
- Deployment process for the booms/truss
- Design of an Attitude Control and Determination System (ADCS) necessary to maintain accurate and repeatable pointing of the spacecraft during and following boom deployment
- Structural, thermal, and electrical designs to account for boom stability, boom rigidity, power, and RF connections along the booms

A number of these technical challenges are reviewed below. A thorough investigation and analysis of these challenges will occur during the proposed Phase II effort, culminating in a overall technology roadmap for implementation. This technology roadmap will provide identification of both existing engineering solutions affecting implementation as well as those enabling technologies for which further development is required, and include corresponding estimates of implementation cost and timeline.

7.2.1 Boom Design and Deployment Concept

The booms/truss components and materials must all be stowed inside the spacecraft until it reaches its desired orbit, due to weight constraints and launch loads. Deployable antennas have been in use since the 1960's. Notably, the Allouette II (ISIS-X) mission used an extendable, tubular mechanism to achieve antenna lengths greater than 70 meters (Figure 15). Recently there has been significant development of metallic and composite materials that can be rolled onto springs and spools for deployment in space (Figure 16). These

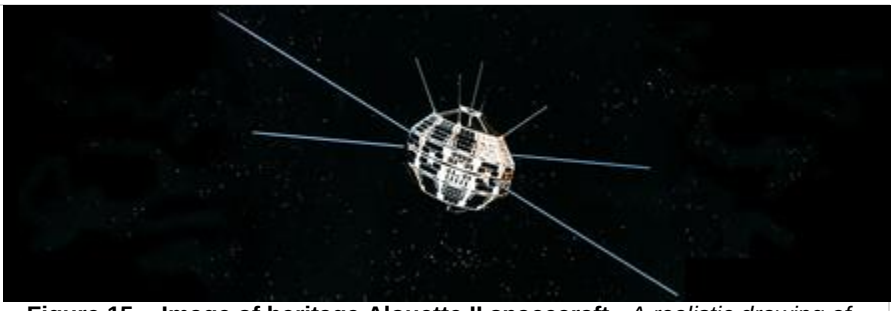

Figure 15: Image of heritage Alouette II spacecraft. *A realistic drawing of faceted circular satellite in empty space. The satellite has eight thin antennas, appearing as wires, protruding radially from the midband of the satellite body. The antenna length appears to be several times the diameter of the satellite body.*

methods offer a lightweight and cost-effective method to effectively store packages of material for large, long baseline deployments. ASTRA is using, and has used in the past, similar deployment methods. Industry partners such as MAA Design, Roccor, and Astro, are continuing to develop new deployable technologies. While those methods have not been tested to the lengths proposed for R-MXAS, we expect they will be scalable to the hundreds of meters required on R-MXAS.

To avoid incursion of the rotating antennas into the antenna beams of some of the static boom antennas, which effect would be detrimental to sensitive RF measurement, we consider a design in which the stationary antenna array boom is displaced to near the lowest point of the rotating arrays (Figure 14)., ASTRA proposes a two-step deployable process for this boom. The first is a comparatively stiff truss (~240 m) that would deploy in the nadir direction. Following, a lightweight motor-driven, tape-spring boom (~240 m) containing the antennas would deploy perpendicularly from the tip of the truss. For deployment of the two rotating booms, each of the rotating booms are envisioned as a single motor-driven, tape-spring hinge deployable boom with a small articulated array of antennas on the tip that would deploy as the booms reach full length. The antennas on the end of the rotating booms need to articulate in order to face nadir continuously, which requires an additional mechanism at the tip of each rotating boom. In the course of the Phase II effort, Leidos and ASTRA will investigate alternate strategies for avoiding beam incursion that may afford a reduced infrastructure implementation.

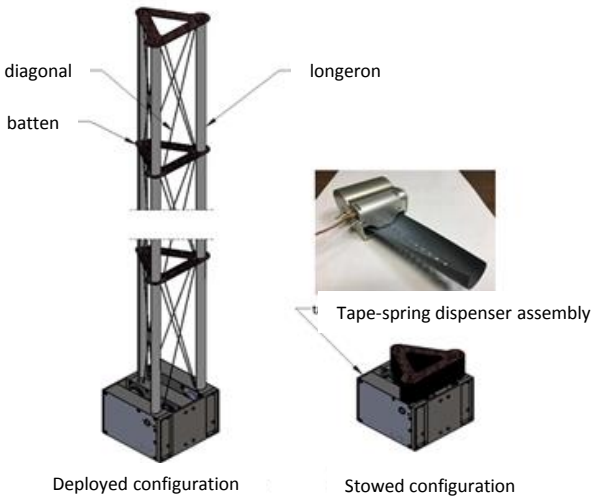

Figure 16: Example boom deployment mechanisms and concepts used by ASTRA on their flight missions. *Three illustrations showing the boom concept at its different stages: a) a deployed triangular-cross-section truss emerging from a base; b) stowed configuration, which is just the base, a small rectangular container; c) photograph of a tape-spring dispenser assembly by which the boom is deployed from its stowed configuration.*

The deployable booms will need to host a number of antennas, while maintaining rigidity without adding unnecessary mass. Current fabrication methods utilize materials such as carbon fiber and spring steel to add rigidity, while minimizing mass. Relative position knowledge of < 2-cm for each antenna is required by science constraints. This position knowledge will be acquired through optical measurements from the spacecraft to retroreflectors attached along the booms.

ASTRA regularly partners with a number of Aerospace vendors (e.g., Roccor, MMA, Tethers Unlimited, and CTD) that are continually developing and advancing the state of the art in deployable fabrication processes. Emerging capabilities in this field include advanced additive manufacturing and automated assembly technologies to enable on-orbit fabrication. Many of these processes may be at high TRL levels by the time of implementation of RMXAS. On-orbit fabrication could play a large part in the ultimate design. All of these potential approaches, along with our described current baseline will be considered in the Phase II effort.

7.2.2 Attitude Control and Determination System (ADCS) Design

The ADCS design is especially challenging due to the large scale of the deployables, and the radical change in spacecraft moments of inertia from pre- to post-deployed configurations. As

the booms must balance the need for rigidity with weight, they will inherently be somewhat flexible and the inertia tensor will not be constant. Additionally, the flexible booms will introduce vibrational modes that need to be accounted for. These vibrational modes may also be excited by station keeping and End of Life (EOL) maneuvers which will affect the accuracy of the maneuver.

The resultant vibrational modes will be identified through a detailed structural analysis, but are expected to be on the order of 1-10 cycles per hour due to the length, and would be validated during ground fabrication and test. The final ADCS functionality and associated on-orbit propulsion capability designs would be tailored to minimize excitation of these modes during operation (e.g., through pulse-width pulse-frequency modulation using input shaping). To combat boom jitter, which may "blur" data acquisition or position knowledge measurements, we will consider approaches such as incorporating dampers between the spinning and stationary parts of the spacecraft. However, it may also be that the flexible booms themselves provide a natural source of energy dissipation and stabilization that dampens jitter sufficiently upon long temporal integrations. It is likely that a combination of natural/passive and active methods of jitter reduction will be required. All of these approaches will be analyzed and compared through a detailed trade study in Phase II, but are not expected to be large design drivers given the expected propulsion and power resources available.

7.3.3 Structural Design

To avoid a collision between the rotating and stationary arrays, they will be spaced far apart in both the horizontal and vertical dimensions so that their closest approach is a few meters. Leidos and ASTRA will collaborate in the investigation of physical design features and innovations by which the baselines not created due to such offsets may be otherwise generated. This will compensate for any unalignment in the motor, and any warping from external forces or differential temperature gradients. A detailed trade study will be conducted in Phase II to determine the lowest SWaP-C balance between lengthening the spacecraft hub and ensuring mechanical alignment.

Since the spacecraft is designed to function in a geostationary orbit, events such as spacecraft retirement must be considered. In order to successfully move the spacecraft to a graveyard orbit above the geostationary belt, the structures must be able to remain intact during times of propulsion. This requirement for structural integrity remains true for any attitude maneuvers and station-keeping burns. This would generally preclude the use of tethers instead of booms in the structure. These processes and potential CONOPS implications will be reviewed in detail in Phase II.

7.2.4 Thermal Design

The thermal design will need a highly-adaptable management approach to account for the varying, large baseline materials found on the booms and the need to minimize changes and deflections. This management will most likely occur through the use of active heaters, coupling paths, and radiators facing deep space on the spacecraft and into the boom elements. Based on specific subsystem thermal operational requirements, thermal paths will be implemented to provide appropriate thermal offloading. Tailoring of thermal link/coupling paths (as an example see Figure 17**)** will occur to supply the appropriate levels of heat transfer between active components/systems and the thermal radiating surfaces.

Figure 17: Example highly conductive thermal link. A photograph a flat rectangular cross-section metal band, with bends applied to the long flat side to form the band into an S-shape, both ends of which are drilled through with a square distribution of four holes, for attachment purposes.

Surface material coatings of appropriate absorption and reflective properties will be analyzed and applied on all spacecraft and boom deployment surfaces. Thermal blankets and Kapton film heaters will be applied to critical subsystems based on operational and survival temperature limits. Temperature sensors will be dispersed throughout the spacecraft and along the booms at key points to monitor the temperatures of components, control heaters, and report any non-optimal subsystem conditions. This will also help enable determination of boom deflection conditions. It is expected that thermal conditions will change considerably between pre- and post-deployment periods and the thermal analysis for on-orbit behavior will be conducted for both periods. As the spacecraft will be in GEO, this static orbit condition will help with long term thermal stability.

To mitigate the effects of thermal expansion and warping on the booms, carbon-fiber composite materials with very low Coefficients of Thermal Expansion (CTE) may be employed. For example, a 50 cm diameter boom with 1° of temperature difference between the front and back sides will warp < 6 cm along its 240 m length if the CTE is kept to ≤ 1e-6. Additional carbon-fiber technologies, coupled with thermal management systems, will be investigated in detail in Phase II.

7.2.5 Electrical Design

The L-band patch antenna sensors will be distributed on the deployable booms. During Phase II, we will examine the optimal method for retrieval of the antenna observations. One approach is to string very small diameter coax cables down the center of the deployed stationary boom from each antenna to a centralized receiver architecture on the stationary spacecraft platform, and similarly on the rotating boom's antennas. While this creates a simplified sampling methodology, with accurate delays being calculated for all coax cable lengths per each antenna and used as correcting factors in the correlation, the current design of the rigid boom has many tens of 69 antennas along the full length, each requiring its own individual cable. Depending on the thickness and rigidity of the deployed boom, this extra mass and volume could result in negative effects on the rigidity and stiffness of the boom. Alternatively, the design could utilize an independent sampling of each antenna by a L-band receiver, and the relevant information for cross-correlation would then be transmitted back to the central spacecraft body through the use of wireless technologies such as WiFi. This would simplify cabling need along the deployed

boom structure, but would require persistent time-keeping management for the sensors to accurately timestamp each sample from its relative antenna prior to transmission, ensuring that the correct timeframe for each sample can be correlated between all of the antennas. Integration of wireless network such as WiFi would also allow for the installation of various sensors, both temperature and gyroscopic, to quantify the deployed boom's state and ensuring accurate knowledge of the location of each antenna relative to the main spacecraft body. This information would be used during science processing to understand the pitch and directionality of the antennas as they look Nadir towards the Earth's disk. The trades between both of these approaches, including key benefits and risks, will be performed during Phase II, with a recommended approach being presented during Phase II.

8.0 OTHER BENEFITS OF THE STUDY

8.1 SCIENTIFIC, ENGINEERING, OR CREATIVE BENEFITS

The R-MXAS concept represents a game-changing approach to achieving effective aperture size well beyond what is currently understood as feasible. The ideas are notably absent from recent surveys of emerging technologies, including as prepared by NASA ESTO ([11]); R-MXAS thus constitutes a disruptive technology idea, strongly warranting investigation. As the Phase I research results described above have demonstrated, the fruits of investigation of a non-(or even anti-) conventional, paradigm-breaking concept and architecture have been not just validation of what was originally proposed, but, precisely because of the "strangeness" of the concept in its departure from the conventional, actual discovery of multiple new and valuable methods and principles. Examples include: a) the interleave / decimate approach to sparsity; b) the TDI-like redundancy array concept; and, most potentially impactful, c) the notion of a high-gain aperture (phased array) at tether-end for boosting radiometric sensitivity of a sparse array. These brand new concepts and methods are likely to find application in endeavors entirely outside the present focus.

8.2 WIDER BENEFITS OF THE STUDY

Additional study of the R-MXAS concept and the potential development efforts that flow from it, have the wider benefit of propelling development into a host of novel sensing concepts serving a diversity of commercial, civil, and military interests. The principals uncovered are likely equally valid in significantly modified architectures, in which, for example, translational motion is exchanged for rotational motion. Potential applications span physical domains (underwater, ground-based (indoor/outdoor), airborne, space), sensor configurations, and sensing modalities (RF, acoustic). Potential examples range from high resolution indoor RF tomographic scanning, for baggage/container inspection or security surveillance purposes, to dramatic enhancement in passive acoustic array synthesis for undersea sensing---the latter an area in which Leidos has already conducted promising R&D.

9.0 REFERENCES AND CITATIONS

1. Y. H. Kerr, P. Waldteufel, J. P. Wigneron, *et al*., "The SMOS mission: New tool for monitoring key elements of the global water cycle," *Proc. IEEE*, vol. 98, no. 5, pp. 666–687, May 2010.
2. J. Font, A. Camps, A. Borges, M. Martin-Neira, J. Boutin, N. Reul, Y. H. Kerr, A. Hahne, and S. Mecklenburg, "SMOS: The challenging sea surface salinity measurement from space," *Proc. IEEE*, vol. 98, no. 5, pp. 649–665, May 2010.
3. J. R. Kendra, "Motion-extended array synthesis, Part 1: Theory and Method", IEEE Trans. Geoscience and Remote Sensing, vol. 55, no. 4, pp. 2028-2044, Apr. 2017.
4. Camps, A. Cardama, and D. Infantes, "Synthesis of large low-redundancy linear arrays," *IEEE Trans. Antennas Propag*., vol. 49, no. 12, pp. 1881-1183, Dec. 2001
5. P. Pal, and P. P. Vaidyanathan, "Nested arrays: a novel approach to array processing with enhanced degrees of freedom," *IEEE Trans. Sig. Proc.*, vol. 58, no. 8, pp. 4167-4181, Aug. 2010.
6. C. Zhang, J. Wu, H. Liu, "Clock scanning microwave interferometric radiometer and potential application analysis," IEEE J. Selected Topics in Applied Earth Observations and Rem. Sensing, Vol. 8, No. 9, pp. 4262-4272, Sept. 2015.
7. C. Zhang, H. Liu, L. Niu, and J. Wu, "CSMIR: An L-band clock scan microwave interferometric radiometer," IEEE J. Selected Topics in Applied Earth Observations and Rem. Sensing, Vol. 11, No. 6, pp. 1874-1882, June 2018.
8. C. Zhang, H. Liu, J. Wu, *et al*., "Imaging analysis and first results of the Geostationary Interferometric Microwave Sounder Demonstrator," *IEEE Trans. Geoscience and Remote Sensing*, vol. 53, no. 1, pp. 207-218, Jan. 2015.
9. X. Guo, H. Liu, et al, "Data processing and experimental performance of GIMS-II (Geostationary Interferometric Microwave Sounder-Second Generation) demonstrator," *2018 IEEE 15th Specialist Meeting on MicroRad*, Mar. 2018.
10. The National Academies, for the 2017-2027 Decadal Survey for Earth Science and Applications from Space, Community Input to ESAS 2017 Request for Information, http://sites.nationalacademies.org/DEPS/esas2017/DEPS_170397
11. "Overview of NASA ESTO Microwave Remote Sensing Investment Strategy Update", NASA ESTO Microwave Technology Community Forum, https://esto.nasa.gov/MicrowaveStrategies/MicrowaveCommunityForumCharts.pdf Mar. 17, 2016.
12. B. Lambrigsten, "GeoSTAR: developing a new payload for GOES satellites," *IEEE Aerospace Conference*, Mar. 2006.
13. A. Tanner, *et al*., "A dual-gain design for the geostationary synthetic thinned array radiometer," *IEEE Geoscience and Remote Sensing Letters*, vol. 11, no. 8, Aug. 2014.
14. C. Zhang, H. Liu, J. Wu, W. Sun, L. Niu, and J. Yan, "A clock scanning aperture radiometer as a potential payload of SPORT", *IGARSS 2014*, pp. 1929-1932, 2014.
15. J. R. Kendra, A. L. Ashworth, T. E. Merryman, A. Fouladi, and N. E. Crow, "Motion-extended array synthesis, Part 2: Experimental validation," *IEEE Trans. Geoscience and Remote Sensing*, vol. 55, no. 4, pp. 2045-2057, Apr. 2017.

16. J. R. Kendra, "Motion-extended array synthesis, Part 3: An offset imaging system perspective", *IEEE Trans. Geoscience and Remote Sensing*, vol. 55, no. 4, pp. 2058-2073, Apr. 2017.